ChemPubSoc Europe

DOI: 10.1002/chem.201803749

Electrocatalysis

Earth-Abundant Transition-Metal-Based Electrocatalysts for Water Electrolysis to Produce Renewable Hydrogen

Ailong Li,[a, b] Yimeng Sun,[a, b] Tingting Yao,*[a] and Hongxian Han*[a, c]

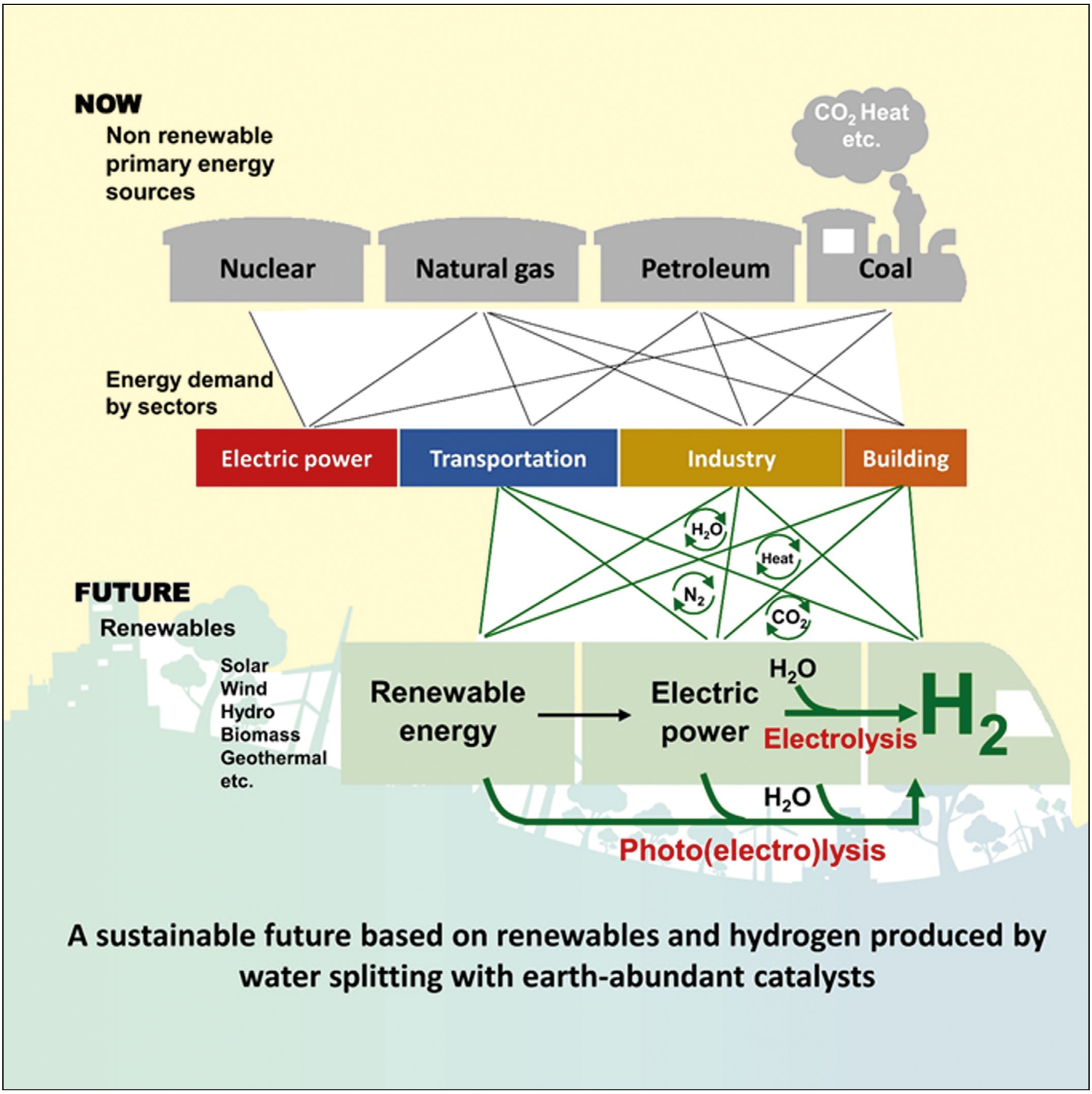

A sustainable future based on renewables and hydrogen produced by water splitting with earth-abundant catalysts

Abstract: Fundamentals of water electrolysis, and recent research progress and trends in the development of earth-abundant first-row transition-metal (Mn, Fe, Co, Ni, Cu)-based oxygen evolution reaction (OER) and hydrogen evolution (HER) electrocatalysts working in acidic, alkaline, or neutral conditions are reviewed. The HER catalysts include mainly metal chalcogenides, metal phosphides, metal nitrides, and metal carbides. As for the OER catalysts, the basic principles of the OER catalysts in alkaline, acidic, and neutral media are introduced, followed by the review and discussion of the Ni, Co, Fe, Mn, and perovskite-type OER catalysts developed so far. The different design principles of the OER catalysts in photoelectrocatalysis and photocatalysis systems are also presented. Finally, the future research directions of electrocatalysts for water splitting, and coupling of photovoltaic (PV) panel with a water electrolyzer, so called PV-E, are given as perspectives.

1. Introduction

Energy and environment are two of the key issues related to the sustainable development of the mankind society.[1] Currently, fossil fuels (oil, coal, and natural gas) still account for more than 85 % of the world energy consumption. Fossil fuels are in fact valuable natural resources for a variety of chemical industry. Combustion of these non-renewable resources as fuels may lead to rapid depletion in the near future. Moreover, the combustion of fossil fuels emits greenhouse gases, such as CO_2, NO_x, and SO_x, that leads to serious environmental problems. Replacement of the fossil energy by renewable and carbon-neutral energy resources is highly desirable.[2]

Solar energy is the only energy resource sufficient to replace fossil fuels. However, owing to the diffusive nature of sunlight, efficient energy capture and storage processes are required for its large-scale utilization.[3] Photovoltaic (PV) cells are capable of converting solar energy into electricity on a large scale, but expensive energy storage devices, such as batteries, are required for the storage and distribution of the electricity. An alternative solution for the storage and distribution of solar energy generated by PV cells is to convert and store solar energy in form of chemical energy, especially in form of H_2. As an energy carrier, H_2 possesses several apparent advantages, such as facile storage and transportation, high energy density (ca. 140 $MJ\,Kg^{-1}$ at 700 atm) and no carbon emission (the only combustion product of H_2 is water).[4]

Not only can H_2 be directly used in hydrogen fuel cell to generate electricity, it is also an important feedstock in chemical industry.[5] PV-electricity-driven water splitting is a promising renewable H_2 production technology, especially if one considers that the PV electricity will be the cheapest technology for electricity generation as the price of the PV electricity is anticipated to be dropped to 0.15 $\$\,kWh^{-1}$ (Data from LONGi Silicon Materials Corp., China).

Coupling of renewable solar PV electricity with a water electrolyzer (PV-E) appears to be one of the most ideal approaches for renewable H_2 production. Current water electrolysis technology includes PEM (proton exchange membrane) water electrolysis, alkaline water electrolysis, and relatively high-temperature solid oxide water electrolysis. The high-temperature solid oxide water electrolysis consumes a lot of energy compared to the other two technologies. Alkaline water electrolysis is already commercialized due to its many advantages, such as using cheap Ni-based catalysts, higher durability due to an exchangeable electrolyte, lower dissolution of the anodic catalyst, and high gas purities due to low gas diffusivity. However, its slow response to operation changes does not make it an ideal candidate to couple with the intermittent and fluctuating renewable energy, such as solar and wind energies. In this regard, coupling PV with a rapid-response PEM water electrolyzer is the most ideal way to produce H_2. However, one of the current bottle-necks for the large-scale application of the PV-PEM is lack of earth abundant oxygen evolution reaction (OER) and hydrogen evolution reaction (HER) catalysts. Usually, noble-metal-based catalysts are used for water electrolysis; for example, IrO_x and RuO_x are used as OER catalysts and Pt/C is used as an HER catalyst in PEM water electrolyzers. In order to facilitate large-scale commercialization of the PV-PEM technology, development of efficient, stable, and low-cost OER and HER catalysts is required.

Considering that both alkaline and acidic PEM water electrolysis can be coupled with PV technology in the near future, in this review, starting from the fundamentals of water electrolysis, we introduce the recent research progresses and trends in the development of earth-abundant first-row transition-metal (Mn, Fe, Co, Ni, Cu)-based OER and HER electrocatalysts working in acidic, alkaline, or neutral conditions. The HER catalysts include mainly metal chalcogenides, metal phosphides, metal nitrides, and metal carbides. As for the OER catalysts, we introduce the basic principles of the OER catalysts in alkaline,

---

[a] *A. Li, Y. Sun, Dr. T. Yao, Prof. H. Han*
State Key Laboratory of Catalysis & Division of Solar Energy
Dalian National Laboratory for Clean Energy
Dalian Institute of Chemical Physics, Chinese Academy of Sciences
Dalian, 116023 (P. R. China)
E-mail: ttyao@dicp.ac.cn
hxhan@dicp.ac.cn

[b] *A. Li, Y. Sun*
University of Chinese Academy of Sciences
Beijing, 100049 (P. R. China)

[c] *Prof. H. Han*
School of Future Technology
University of Chinese Academy of Sciences
Beijing, 100049 (P. R. China)

The ORCID identification number(s) for the author(s) of this article can be found under:
https://doi.org/10.1002/chem.201803749.

Part of a Special Issue focusing on topics within the field of renewable energy. To view the complete issue, visit Issue 69.

acidic, and neutral media, followed by the discussion of the Ni, Co, Fe, Mn, and perovskite type OER catalysts. The different design principles of the OER catalysts in photoelectrocatalysis and photocatalysis systems are also presented. Finally, perspectives for future research directions are given. We hope this Minireview can spark more ideas in the development of earth-abundant-element electrocatalysts for water electrolysis, and hence the dream of large-scale production of renewable H_2 comes a step nearer.

2. Fundamentals of Water Electrolysis

Electrochemical water splitting involves two crucial half-cell reactions, cathodic hydrogen evolution reaction (HER) and anodic oxygen evolution reaction (OER) [Eqs (1) and (2)].

$$\text{HER (cathode)}: \; 2\,H^+(aq) + 2\,e^- \rightarrow H_2(g),\; E^0_{HER} = 0.00\,V \qquad (1)$$

$$\text{OER (anode)} \; 2\,H_2O(l) \rightarrow O_2(g) + 4\,H^+(aq) + 4\,e^-,\; E^0_{OER} = 1.23\,V \qquad (2)$$

Splitting water into hydrogen and oxygen is not thermodynamically favorable at standard temperature and pressure. A standard Gibbs free energy of at least $\Delta G^0 = +237.2\,kJ\,mol^{-1}$, which is equivalent to $E^0 = 0.00$ V (vs. normal hydrogen electrode (NHE)), is required for electrolyzing water. According to the Nernst equation, the thermodynamic equilibrium potentials are $E^0_{HER} = 0.00$ V for the water reduction reaction and $E^0_{OER} = 1.23$ V for the water oxidation reaction.

However, in the real water electrolysis process, an extra energy called the overpotential (η) is required to overcome the high activation energy, sluggish kinetics, poor energy efficiency, and some other adverse issues. Then, the actual applied potential for the two half-cell reactions of water splitting can be expressed as Equations (3) and (4), in which iR is the ohmic potential drop of the system and η is the overpotential, which directly determines the energy efficiency of the electrolyzer. By using the active electrocatalysts, the overpotential of the HER and OER can be significantly reduced.[6]

$$E_{HER} = E^0_{HER} + iR + \eta_{HER} \qquad (3)$$

$$E_{OER} = E^0_{OER} + iR + \eta_{OER} \qquad (4)$$

Aiming to evaluate the catalytic activities of electrocatalysts, several parameters can be calculated from the measured performance curves. The overpotential at a certain current density can be directly observed from the iR-corrected current–potential curves (Figure 1 a). The Tafel slope is commonly used to indicate the intrinsic properties of an electrocatalyst. The Tafel equation is shown as follows is given in Equation (5), in which η is the overpotential, j is the current density, j_0 is the exchange current density, and b is the Tafel slope.

$$\eta = b \log(j/j_0) \qquad (5)$$

The Tafel plots can be calculated from the iR-corrected current–potential curves according to the Tafel equation. Then, the slope of the linear part of Tafel plots will give the value of b for an electrocatalyst (Figure 1 b). The potential at which the linear Tafel region begins is referred as onset potential for OER.[7] Extrapolating the linear Tafel region to the lateral axis will give the value of exchange current density, which also can

Ailong Li received his Bachelor degree from the Ocean University of China. He is currently a Ph.D. candidate in Dalian Institute of Chemical Physics, Chinese Academy of Science. His research interest is in the in the fundamental understanding and development of junction-based photo(electro)catalysts.

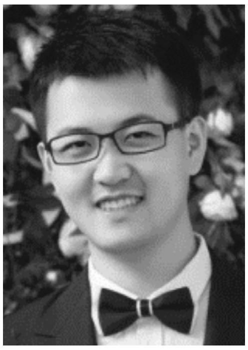

Yimeng Sun received her Bachelor degree in Chemistry from Zhengzhou University in 2016. She is currently a Ph.D. candidate of State Key Laboratory of Catalysis, Dalian Institute of Chemical Physics under the supervision of Prof. Can Li and Prof. Hongxian Han. Her research focuses on the electrocatalysts for water splitting.

Dr. Tingting Yao is an Associate Professor in the State Key Laboratory of Catalysis at Dalian Institute of Chemical Physics. She received her Ph.D. in Industrial Catalysis from the South China University of Technology, and her Bachelor's degree in Pharmaceutical Engineering from Zhengzhou University. She did her postdoctoral work at Dalian Institute of Chemical Physics in 2013–2017. Her current research focuses on the water splitting reaction and the interfacial physics and chemistry of composite photoelectrodes for solar energy conversion.

Prof. Hongxian Han received his Ph.D. degree in chemistry from the University of New South Wales, Sydney, Australia in 2003. He was a postdoctoral fellow/project research scientist in Lawrence Berkeley National Laboratory till 2009. Currently, he is a professor in Dalian Institute of Chemical Physics, Chinese Academy of Sciences, and also a professor in School of Future Technology, University of Chinese Academy of Sciences. His major research interest is in artificial photosynthesis of solar fuels, with great emphasis on understanding the mechanism of water splitting and CO_2 reduction reactions.

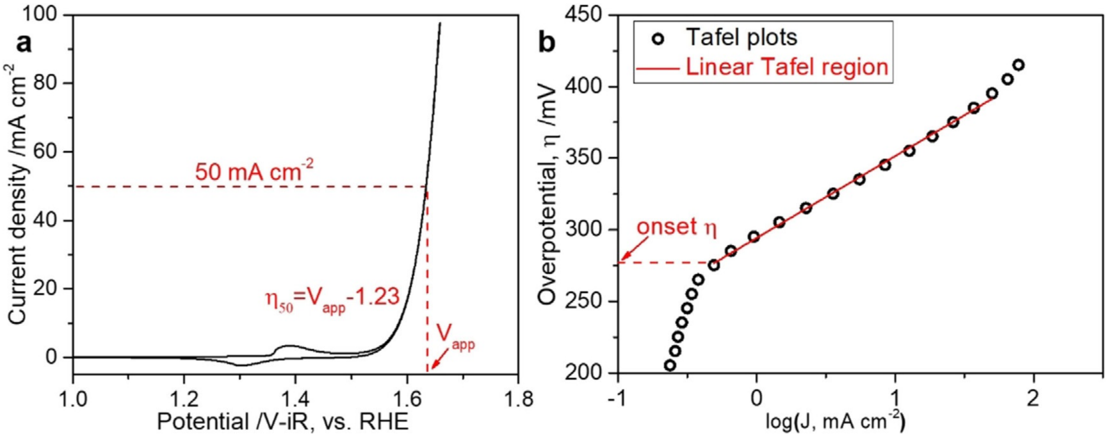

Figure 1. a) Cyclic voltammetry curve of anode for OER after *iR* correction. V_{app} is the applied potential, and η_{50} is the overpotential at current density of 50 mA cm^{-2}. b) Tafel plots of anode for OER.

be used to describe structural, physical, or surface properties and other factors that influence the electron transfer at electrode/electrolyte interface.[8]

3. Hydrogen Evolution Catalysts

Water reduction is an important step to realize clean hydrogen production. The half-reactions can be expressed by Equations (6) and (7).

$$\text{Acidic solution}: \ 2H^+ + 2e^- \rightarrow H_2 \qquad (6)$$

$$\text{Neutral or alkaline solution}: \ 2H_2O + 2e^- \rightarrow H_2 + 2OH^- \qquad (7)$$

In acidic media, the HER mechanism involves three elementary reaction steps. The first one is the Volmer step ($H^+ + e^- \rightarrow H^*$), in which a proton reacts with an electron to generate an adsorbed hydrogen atom (H*) on the cathode surface. The free energy of hydrogen adsorption (ΔG_H) is used to describe the interaction strength of H* with the electrode surface. A moderate value of ΔG_H will benefit the following Tafel step ($2H^* \rightarrow H_2 + 2^*$) or Heyrovsky step ($H^* + H^+ + e^- \rightarrow H_2$) or both (Figure 2 a).[9]

In alkaline media, the Volmer–Tafel process or Volmer–Heyrovsky process could be described by Equations (8–10).[11]

$$\text{Volmer step}: \ H_2O + e^- \rightarrow H^* + OH^- \qquad (8)$$

$$\text{Tafel step}: \ 2H^* \rightarrow H_2 + 2^* \qquad (9)$$

$$\text{Heyrovsky step}: \ H^* + H_2O + e^- \rightarrow H_2 + OH^- \qquad (10)$$

The adsorption of the H_2O molecule is involved in these pathways. The adsorbed H_2O molecule is electrochemically reduced into an H atom and adsorbed OH^-, which should be desorbed in soon to fresh the surface sites and allow the formation of H* for H_2 generation. Thus, the formation and desorption of OH^- species might be the control steps for hydrogen evolution reaction in alkaline media.[12]

The volcano plots are usually used to illustrate the relationship between the electrocatalytic activity and the ΔG_H of adsorbed atomic hydrogen (Figure 2 b).[10] A ΔG_H value of nearly zero is given for the reported best solid-state Pt hydrogen evolution catalyst (HEC). Too weak ($\Delta G_H < 0$) or too strong ($\Delta G_H >$

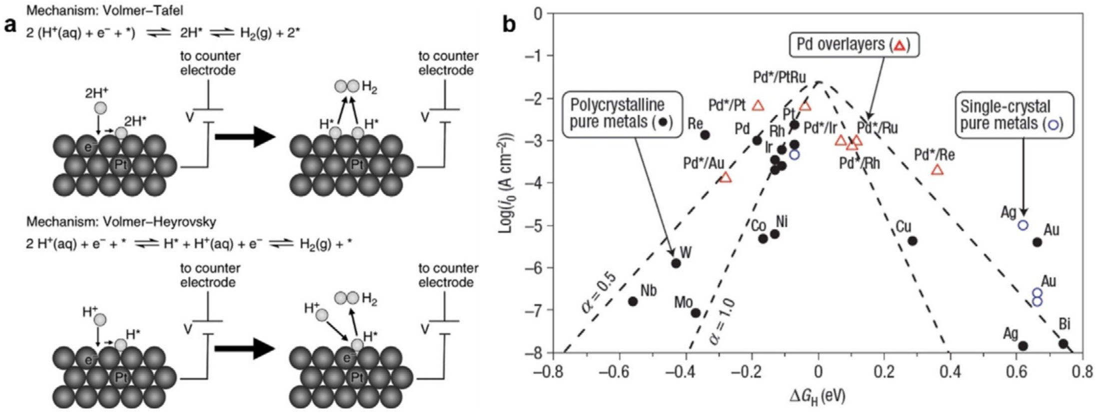

Figure 2. a) Schematic illustration of the HER mechanisms. The asterisk (*) represents a free active site and H* indicates the hydrogen atom bounded to the active site. Reproduced with permission from reference [9]. Copyright 2012, American Chemical Society. b) Volcano plots for the hydrogen evolution reaction. Reproduced with permission from reference [10] Copyright 2006, Nature Publishing.

0) binding energies of H* are not desired. The former case will result in a slow Volmer step and limit the overall turnover rate. In the case of the latter, the bonding of H* is too strong with the electrode to make an easy Volmer step, and then harms the subsequent Tafel or Heyrovsky steps.[13] Thus, the noble-metal-free hydrogen evolution catalyst should possess an approximately zero ΔG_H. Most of the active HECs are mainly consisted by transition-metal elements (e.g., Fe, Co, Ni, Cu, Mo, and W) and the non-metal elements (e.g., B, C, N, P, S, and Se). In the followings, the crystal structure, and electronic and surface properties of catalysts are elaborated to disclose the factors in favor of the HER activity.

3.1. Metal chalcogenides

The appearance of metal chalcogenides has had a profound impact on the development of noble-metal-free hydrogen evolution catalysts. One representative type is layered transition-metal chalcogenides with the composition of MX_2 (M=Mo or W and X=S or Se) exhibiting 1T (tetragonal, AA stacking), 2H (hexagonal, ABAB stacking) or 3R (rhombohedral, ABCABC stacking) polymorphs (Figure 3). The first two phases are commonly seen in chalcogenide catalysts for water electrolysis. The 1T polymorph is a metallic X-M-X single layer, which consists of edge-sharing MX_6 octahedra. The 2H phase is constructed by several X-M-X layers built from edge-sharing MX_6 trigonal prisms.[14]

In 2005, Nørskov and co-workers showed that the calculated free energy for hydrogen evolution on MoS_2 was similar to that of Pt (Figure 4a), and experimentally verified the activity of MoS_2 for the hydrogen evolution reaction.[15] Layered MoS_2 exhibits two kinds of surface site, terrace sites on the basal plane and edge sites on the edge of the nanomaterial. Regardless of particle size, the electrocatalytic hydrogen evolution activity of MoS_2 has been found to correlate linearly with the number of its edge sites. It indicates that the edge sites of the MoS_2 are highly catalytically active.[16] Aiming to expose more active edge sites, Jaramillo and co-workers synthesized an MoS_2 material with highly ordered mesoporous architecture, and fabricated large-area contiguous thin films with variable thickness (Figure 4c). The total HER activity of this mesoporous MoS_2 material was largely enhanced along with the increased surface area and the active sites per surface area (Figure 4b).[17]

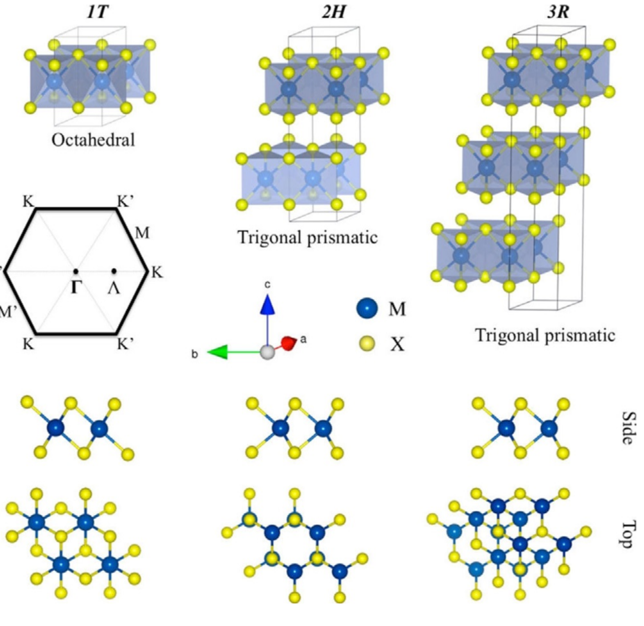

Figure 3. Layered structure of transition-metal chalcogenides with a composition of MX_2. Reproduced with permission from reference [14]. Copyright 2015, American Chemical Society.

The 2H phase is usually thermodynamically favored for MoS_2 semiconductors. However, the poor conductivity along the *c* crystallographic axis of the bulk layered MoS_2 disfavors the long-range electron conduction and its electrocatalytic activity. By using a lithium intercalation method, semiconducting 2H-MoS_2 was chemically exfoliated into 1T-MoS_2 metallic nanosheets to enhance the electrical transport and density of active sites. The obtained 1T-MoS_2 nanosheets had a Tafel slope of 43 $mV\,dec^{-1}$, indicating facile electrode kinetics for the hydrogen evolution reaction.[18] Wang and co-workers have investigated the kinetic barriers of MoS_2-based catalysts for H_2 evolution through the Tafel mechanism. An extremely low Tafel slope of 30 $mV\,dec^{-1}$ can be expected for MoS_2 nanowires grown on Au(755) surfaces according to a calculated kinetic barrier of 0.49 eV on the Mo edges, suggesting the Volmer–Tafel mechanism. Ni(755) and Cu(755) were predicted to act as the alternative substrates of Au(755) to support MoS_2 and maintain the same activity.[19]

There are also some different viewpoints of MoS_2 active sites. Chhowalla and co-workers noticed that electrochemical oxidation of the edge sites played less impact on catalytic activity of 1T-MoS_2 than 2H-MoS_2, suggesting the catalytical activity of basal plane. Meanwhile, they emphasized the critical role of charge-transfer kinetics in promoting the hydrogen evolution activity of MoS_2.[20] Other researchers have mentioned that thermodynamically stable defects existed in the metallic twin boundaries of slightly Mo-enriched $MoTe_2$ and some other chalcogenides, endowing the basal plane of the 2H phase with a high HER activity.[21]

The unfavorable impact of low electrical conductivity on MoS_2 activity can be adjusted through constructing hetero-nanostructures. Vertically oriented MoO_3 nanowires with a diameter of about 20–50 nm have been used as cores to support an MoS_2 shell about 2–5 nm in thickness. The conductive MoO_3 core enabled facile charge transport, and the ultrathin MoS_2 shell facilitated the HER kinetics.[22] The MoS_2 catalysts were also deposited on a graphene-coated 3D Ni foam. The obtained Ni foam/graphene/MoS_2 3D catalysts showed a Tafel slope of 42.8 $mV\,dec^{-1}$ for the hydrogen evolution reaction, and a hydrogen evolution rate of 13.47 $mmol\,g^{-1}\,cm^{-2}\,h^{-1}$ at a certain overpotential (0.2 V).[23] A low Tafel slope of 40 $mV\,dec^{-1}$ was realized on the N-doped carbon-nanotube-supported MoS_2 catalyst.[24] Recently, zero-valent metals (Pt, Ru, Pd, and Au) have been encapsulated in the layered MoS_2 to form metal-intercalated MoS_2. Confined Pt nanoparticles within the MoS_2 (Pt-MoS_2) presented a Tafel slope of 25 $mV\,dec^{-1}$, which was comparable to that of 40 % Pt/C (22 $mV\,dec^{-1}$).

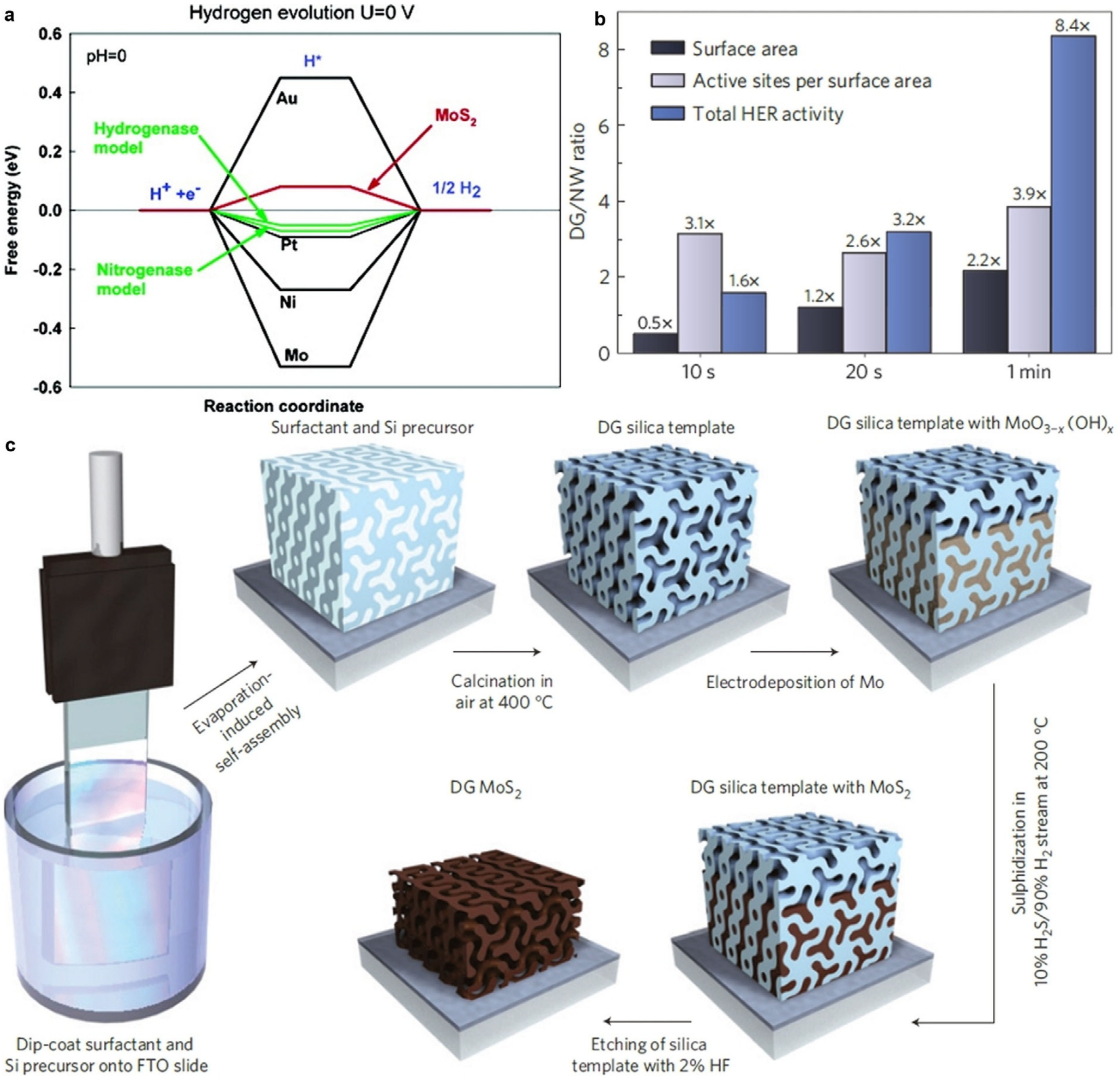

Figure 4. a) Calculated free energy diagram for hydrogen evolution. Reproduced with permission from reference [15]. Copyright 2005, American Chemical Society. b) Surface area, active sites per surface area and HER activity of the MoS_2 catalysts. c) Synthesis process of mesoporous MoS_2 electrocatalyst. Reproduced with permission from reference [17]. Copyright 2005, Nature Publishing.

Meanwhile, the Pt-MoS_2 material has the highest stability (ca. 35 h) for hydrogen evolution compared with the other catalysts (40% Pt/C, Ru-MoS_2, Pd-MoS_2, Au-MoS_2).[25] Bae and Ho have reported bulk layered heterojunctions of Cu-Mo-S or Ni-Mo-S, which consist of uniformly dispersed MoS_2 or NiS_2 in the Cu_2S matrix. An asymmetric charge transfer through layered frameworks was expected in the resulting heterojunctions. The Cu-Mo-S hetero-catalyst exhibited a Tafel slope of 30–40 mV dec^{-1} for hydrogen evolution. The obtained Ni-Mo-S catalyst could sustain a stable HER operation over 10 days in 1 M KOH.[26]

Apart from MoS_2 materials, $MoSe_2$ films also proved to exhibit layered structure and comparable catalytic activities to that of MoS_2 for hydrogen evolution reactions.[27] Aiming to increase the electrocatalytic HER activity, edge-rich structures can be formed through constructing a solid solution of MoS_2 and $MoSe_2$. The Se-rich $MoS_{2-x}Se_x$ was expected to have a relatively lower hydrogen adsorption free energy than that of its S-rich counterparts. The Tafel slopes varied from 82 mV dec^{-1} (MoS_2) to 48 mV dec^{-1} ($MoS_{0.8}Se_{1.2}$).[28]

Chemical exfoliation can also be used to prepare monolayered WS_2 nanosheets, which exhibited considerable activity for hydrogen evolution reaction even under very low overpotentials (80–100 mV) with a Tafel slope of 55 mV dec^{-1}. A high concentration of strains, caused by zigzag-like local lattice distortions in metallic 1T-WS_2 nanosheets, was assumed important for facilitating hydrogen evolution reaction (Figure 5).[29] The WS_2/WS_3 material was synthesized through an electrochemical method. The obtained product possessed a composition of $WS_{2.64}$ and a chain-like structure consisting of S^{2-} and S_2^{2-} li-

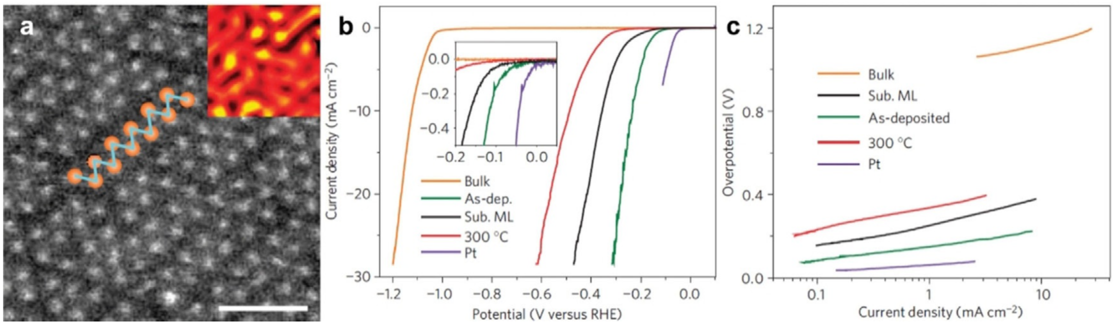

Figure 5. a) High-resolution STEM images of 1T-WS2 monolayer. (inset: the strain tensor map obtained from STEM-HAADF image. Scale bar: 1 nm). b) Linear scan voltammetry curves and c) Tafel plots of Pt nanoparticles, 2H-WS_2 (300 °C), sub-monolayer, as-exfoliated and bulk WS_2. Reproduced with permission from reference [29]. Copyright 2013, Nature Publishing.

gands, leading to different metal–chalcogen binding strengths in the $WS_{2.64}$ electrocatalyst. The varied W—S binding strengths made it possible to simultaneously adsorb and desorb the active species on separate active sites of $WS_{2.64}$. The $WS_{2.64}$ electrocatalyst presented a Tafel slope of 43.7 mV dec^{-1}, suggesting a fast reaction kinetics for hydrogen evolution.[30]

Layered WSe_2 films were also reported to be active for water reduction. The Tafel slope (77.4 mV dec^{-1}) of WSe_2 on carbon fiber paper was a little larger than that of the $MoSe_2$ counterparts (59.8 mV dec^{-1}), suggesting a relatively slow HER kinetics on WSe_2 surface.[31] The hydrogen adsorption free energy of the WSe_2 on the basal plane was assumed to vary with the Se vacancy concentration. The electrocatalytic activity of the WSe_2 was adjusted by controlling Se vacancies on the basal planes through the annealing approach under different temperatures. The optimized WSe_2 catalyst displayed an onset potential of 195 mV and a Tafel slope of 76 mV dec^{-1}.[32] Yang and co-workers have synthesized a mix-phased $W(Se_xS_{1-x})_2$ nanoporous material, which exhibited catalytically active defects due to the lattice mismatch and disordering. The conducting 1T phase in the strained architecture enabled facile electron transfer during catalytic reactions. The $W(Se_xS_{1-x})_2$ catalyst showed an onset overpotential of 45 mV and a Tafel slope of 59 mV dec^{-1}.[33] The surface coordinated environment and ligand also impact the d-band center of the transition-metal atoms and, therefore, the hydrogen adsorption free energy or reaction kinetics on the WSe_2 catalysts.[34]

The first-row transition-metal dichalcogenides (MX_2, M = Fe, Co, Ni and X = S or Se) can also be used to construct active non-precious HER catalysts. The metal atoms of dichalcogenides are bound with six adjacent S or Se atoms to form the MX_6 octahedron, which are connected into corner-shared cubic pyrite-type or edge-shared orthorhombic marcasite-type structures (Figure 6).[35] As shown in Figure 2 b, Ni metal has a similar ΔG_H value to that of Pt, but Ni usually presents worse catalytic activity for hydrogen evolution reaction. This could be attributed to the strong adsorption of OH^- on Ni metal, blocking the surface sites for the H* formation. After constructing a NiO/Ni structure, the charged Ni^{2+} species with unfilled d-orbital could facilitate the attachment of OH^- on NiO site at the interface, meanwhile, H* could be formed on a nearby Ni site. The obtained NiO/Ni-CNT catalyst could achieve a photocurrent density of about 20 mA cm^{-2} at 1.5 V and a Tafel slope of 82 mV dec^{-1} for hydrogen evolution reaction.[36] The Tafel slope of 82 mV dec^{-1} indicates a slow Tafel or Heyrovsky step during water reduction. A smaller Tafel slope (ca. 40–60 mV dec^{-1}) can be achieved on nickel dichalcogenides (NiS_2, $NiSe_2$). By using the electronegativity and principle quantum number of anion X as the important descriptors, the Ni-Ni_3S_2 catalyst with a surface S:Ni atomic ratio of 28.9 % was evaluated to exhibit the best catalytic activity and lowest charge-transfer resistance among the nickel-based compounds for the hydrogen evolution reaction.[37]

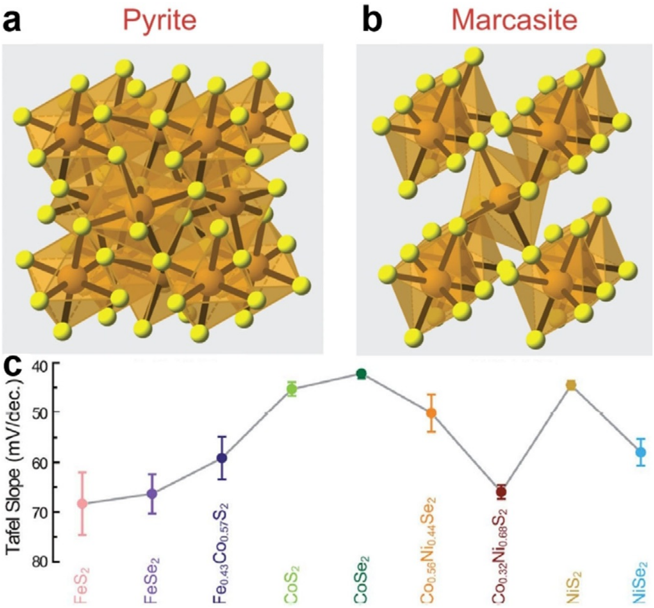

Figure 6. Crystalline structure of transition metal chalcogenides. a) Pyrite-type crystal structure. b) Marcasite-type crystal structure (metal atoms: orange, S or Se atoms: yellow). c) Summary of Tafel slopes of transition metal chalcogenide catalysts. Reproduced with permission from reference [35]. Copyright 2013, Royal Society of Chemistry.

In the MX_6 octahedron unit, the 3d bands of the metal atoms were split into t_{2g} and e_g sub-bands. The d-electron configuration of transition metal cations will largely impact the catalytic activities of the metal chalcogenides. The Co 3d electrons in $CoSe_2$ exhibit a low-spin $t_{2g}{}^6e_g{}^1$ configuration, making

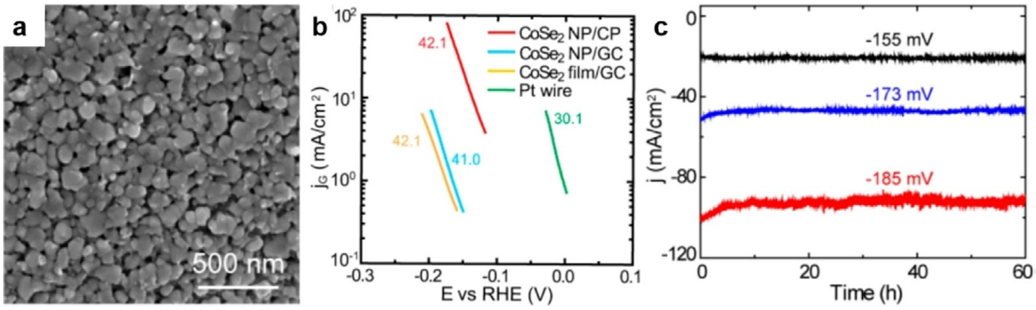

Figure 7. a) SEM image of $CoSe_2$ catalyst. b) Tafel slopes of $CoSe_2$ nanoparticle (NP) or film on carbon fiber paper (CP), glassy carbon (GC) electrodes. c) Time dependence of cathodic current density during electrolysis over 60 h at fixed overpotentials of −155, −173, and −185 mV (after *iR* correction), respectively. Reproduced with permission from reference [38]. Copyright 2014, American Chemical Society.

$CoSe_2$ a metallic conductor and benefiting the charge transfer from electrode to the catalyst surface. A small Tafel slope of 41 mV dec^{-1} was reported for the $CoSe_2$ nanoparticles measured with glassy carbon electrode, suggesting a Volmer–Heyrovsky HER mechanism.[39] This $CoSe_2$ electrode can sustain a long-term hydrogen evolution operation for over 60 h in acid solution (Figure 7).[38] Substitution of anion Se with P can also modulate the electronic configuration of the catalysts and lower the hydrogen adsorption energy on active sites, facilitating the desorption of hydrogen on the catalysts and resulting in enhanced catalytic activities for HER.[40] Tightly connected $Co_{0.85}Se$ nanocrystals were homogeneously anchored on graphene nanosheets to form a porous and conductive $Co_{0.85}Se$/graphene electrocatalyst. The hybrid $Co_{0.85}Se$/graphene catalyst had a low Tafel slope of 34.4 mV dec^{-1} compared with that of unhybridized $Co_{0.85}Se$ (41.8 mV dec^{-1}), suggesting a Volmer–Tafel combination.[41]

Iron chalcogenides usually presented relatively low HER activities, but a longer stability up to several days in neutral pH conditions, compared to its molybdenum, cobalt, or nickel-based counterparts.[42] Leonard and co-workers have synthesized low-dimensional FeS_2 nanostructures and found that the 2D FeS_2 discs exhibited the highest electrocatalytic activity compared to the 1D FeS_2 nanowires and 3D FeS_2 cubes. The 2D FeS_2 discs showed a Tafel slope of 76 mV dec^{-1} and an exchange current density of 1.7 uA cm^{-2} in pH 7 phosphate buffer solution for hydrogen evolution reaction.[43] Suib and co-workers have synthesized a mesoporous FeS_2 electrocatalyst for the hydrogen evolution reaction through a template-free method. The mesoporous FeS_2 exhibited a higher surface area of 128 m^2 g^{-1} compared with commercial one (<1 m^2 g^{-1}) and enhanced the exposure of (210) surfaces. According to the DFT results, the (210) surfaces have a lower activation barrier and be more favorable for O–H bond cleavage of water molecule relative to the (100) surfaces. Then, a low overpotential of 96 mV was required for the FeS_2 to achieve a HER current density of 10 mA cm^{-2}, meanwhile, a Tafel slope of 78 mV dec^{-1}.[44] Introducing Mo to form Mo–Fe selenide could modulate the electronic properties of the heterointerface and accelerate electron transfer from $FeSe_2$ to the active sites of 1T-$MoSe_2$, facilitating the HER kinetics and resulting in a small Tafel slope of 57.7 mV dec^{-1}.[45] Coupling Co with Fe to form $Fe_{0.7}Co_{0.3}Se_2$ could also adjust the electronic structure of the catalysts and decrease the Tafel slope for HER from 84 mV dec^{-1} of $FeSe_2$ to 51 mV dec^{-1} of $Fe_{0.7}Co_{0.3}Se_2$ catalysts. The reduced graphene oxide (rGO) substrate further enlarged the surface area and enhanced charge transport during electrocatalytic reactions. The $Fe_{0.7}Co_{0.3}Se_2$/rGO hybrid material presented an extremely low Tafel slope of about 36 mV dec^{-1} for hydrogen production.[46]

3.2. Metal phosphides

Transition-metal phosphides (M_xP_y, M = Fe, Co, Ni, Cu, Mo and W) are also the promising noble-metal free catalysts for the hydrogen evolution reaction. They can sustain high activity, high stability, and about 100 % Faradic efficiency for hydrogen evolution in solution with any pH value. Effectively trapping protons, bonding atomic hydrogen, and desorption of H_2 are the key characteristics for a good HER catalyst. It is known that [NiFe] hydrogenases are quite active for the catalysis of the hydrogen evolution reaction at room temperature. Liu and Rodriguez have investigated the kinetics of the HER on the hydrogenase and its analogues, listing a sequence of calculated catalytic activities as follows: [NiFe] hydrogenase > $[Ni(PNP)_2]^{2+}$ > Ni_2P (001) > $[Ni(PS3^*)(CO)]^{1-}$ > Pt (111) > Ni (111) (Figure 8 a). Ni_2P displays a superior activity over the bulk Pt and Ni surfaces. The authors mentioned that the hydrogen bonding on metal (Pt, Ni) hollow sites is too strong to benefit the H_2 removal. Whereas in Ni_2P, the concentration of highly active Ni sites was decreased due to partly poisoned by the strong H–Ni interaction on surface and the presence of P atoms, which may also lead to the moderate bonding to the intermediates and products.[47] It can be seen from the crystal structure that the Ni_2P (001) surface exposes Ni and P sites with structural and electronic analogies to the active site of [NiFe] hydrogenase (Figure 8 b), whereby providing proton–acceptor and hydride–acceptor centers for facile hydrogen evolution process.[48] As a result, Ni_2P has the potential to be a good catalyst for hydrogen evolution. Further investigation carried by Dismukes and co-workers showed that Ni_5P_4 exhibited higher TOFs than that of Ni_2P in both acid and alkaline media. The Ni_5P_4 nanocrystals also exhibit low electrical impedance losses and high corrosion resistance during water reduction. Crystalline Ni_5P_4 has an extremely small Tafel slope of 33 mV dec^{-1}

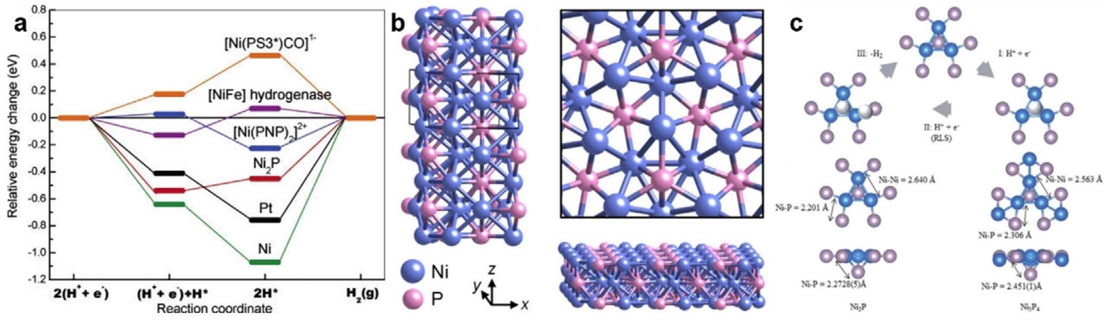

Figure 8. a) Calculated energy changes for the HER on different catalysts surfaces. Reproduced with permission from reference [47]. Copyright 2005, American Chemical Society. b) Crystal structure of Ni_2P. Reproduced with permission from reference [48]. Copyright 2013, American Chemical Society. c) Reaction mechanism, structural of the proposed active site on Ni_2P [001] and Ni_5P_4[001]. Reproduced with permission from reference [49]. Copyright 2015, Royal Society of Chemistry.

and an overpotential of 62 mV at 100 mA cm^{-1} in acid solution.[49] The three-step HER mechanism in acid on Ni_2P [001] is shown in Figure 8c. The rate-limiting step for HER is identified as the second electron-transfer step (step II) to a bridging proton at a Ni—P bond. The longer Ni—P bond length of Ni_5P_4 allows increased overlay of the H 1s orbital with Ni valence orbitals, leading to an increased covalent interaction and making the first electron transfer more favorable. This gives a significant prospect to develop the noble-metal-free HER catalyst for the replacement of Pt.

Schaak and Lewis have synthesized uniform, multi-faceted CoP nanoparticles through reacting Co nanoparticles with trioctylphosphine. The obtained CoP/Ti electrode showed an overpotential of 85 mV at a cathodic current density of 20 mA cm^{-2} and a Tafel slope of 50 mV dec^{-1}, indicating a relatively slow HER kinetics. However, the HER exchange current density (ca. 1.4×10^{-4} A cm^{-2}) of the CoP catalyst was comparable to that of Ni_2P nanoparticles for hydrogen evolution in acid solution.[48] Ruthenium was introduced to form RuCoP clusters by Liu and co-workers. The Tafel slopes of RuCoP decreased to about 31–37 mV dec^{-1}, indicating a Tafel or Heyrovsky step limited the hydrogen evolution process in acidic or alkaline solutions. The hybrid RuCoP clusters also gave a considerably high TOF value of 10.95 s^{-1} in acid media and 7.26 s^{-1} in alkaline media at an overpotential of 100 mV.[50]

The different degrees of phosphorization on metal element may lead to metal phosphides with diverse catalytic activities. Figure 9a shows the structural evolution of Mo phosphide during phosphorization. The obtained MoP presents the best catalytic hydrogen evolution activity among the Mo-based electrocatalysts. It shows a Tafel slope of 54 mV dec^{-1} in acidic media. According to the DFT calculation results, P atoms, which exhibited a nearly zero Gibbs free energy, were identified as the active site and responsible for creating a high concentration of active edges for HER.[51] Wang and Liang have uniformly deposited MoP nanoparticles on carbon nanotubes. The small particle size and high crystallinity of MoP were critical for improved charge transfer and sustained high dispersion during HER.[52]

In contrast, tungsten phosphide and copper phosphide were usually less active for hydrogen evolution compared with the metal phosphides mentioned above. WP nanorod arrays on carbon cloth (WP NAs/CC) were synthesized through phosphorization of the corresponding WO_3 precursor. The WP NAs/CC electrode needed an overpotential of 130 mV to afford a HER current density of 10 mA cm^{-2} and presented a Tafel slope of 69 mV dec^{-1} in acid solution. This catalyst can also be operated in neutral and alkaline media to realize water reduction reaction; however, the Tafel slope increased to 125 mV dec^{-1} and 102 mV dec^{-1}, respectively.[53] Lewis and Schaak have reported Ti-foil-supported amorphous WP nanoparticles (WP/Ti) that can provide a current density of 10 mA cm^{-2} at an overpotential of 120 mV.[54] Sun and co-workers have found that the bulk WP_2 exhibited a high HER Tafel slope of 107 mV dec^{-1}, which was observed to decrease to 57 mV dec^{-1} with WP_2 submicroparticles. A low onset overpotential of 54 mV was enough for the WP_2 submicroparticles to drive the hydrogen evolution reaction, and an overpotential of 161 mV was needed to afford a current density of 10 mA cm^{-2}. The WP_2 submicroparticles showed a Tafel slope of 57 mV dec^{-1} for water reduction in acid solution.[55]

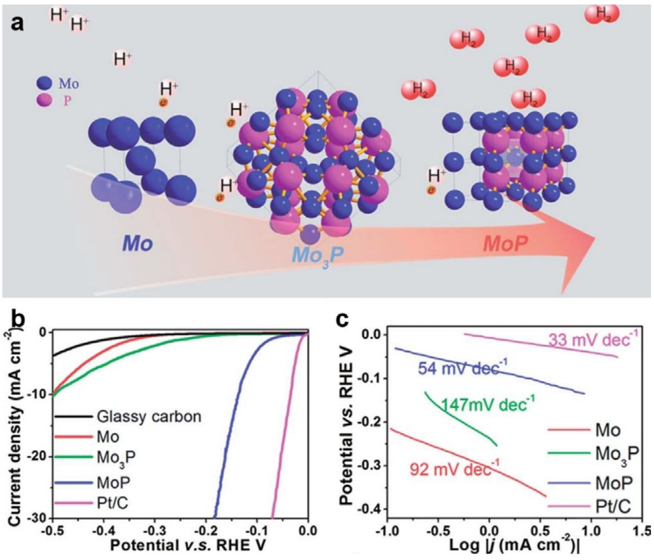

Figure 9. a) The structural evolution of Mo phosphide during phosphorization. b) Linear sweep voltammetry curves and c) Tafel slopes of Mo, Mo_3P and MoP in acidic solution. Reproduced with permission from reference [51]. Copyright 2014, Royal Society of Chemistry.

Recently, heteroatoms were introduced to adjust the catalytic activities of tungsten phosphide. Kuang and Su have obtained a porous molybdenum tungsten phosphide (Mo-W-P) hybrid nanosheet, which can afford a high current density of 100 mA cm^{-2} under a low overpotential of 138 mV and a smaller Tafel slope of 52 mV dec^{-1} compared with that of MoP (55 mV dec^{-1}) and WP$_2$ (78 mV dec^{-1}) catalysts. This showed the advantages of the synergistic effects between Mo and W atoms in improving the intrinsic catalytic activities of the catalysts.[56] S-Doped CoWP nanoparticles encapsulated in an S- and N-doped carbon matrix (S-CoWP@(S, N)-C) were reported to have a ΔG_H value (0.050 eV) close to that of Pt (zero). The S-CoWP@(S, N)-C electrocatalyst realized a current density of 10 mA cm^{-2} under low overpotentials of 35 mV and 67 mV in acid and alkaline medias. A small Tafel slope of 35 mV dec^{-1}, which is comparable to that of Pt/C, was also observed for the S-CoWP@(S, N)-C catalyst, indicating a Heyrovsky–Tafel limiting HER process.[57] Wang and co-workers also reported iron-doped WO$_x$P nanoplates on a reduced graphene oxide support (Fe-WO$_x$P/rGO) that can achieve a current density of 10 mA cm^{-2} under a low overpotential of 54.6 mV and a small Tafel slope of 41.99 mV dec^{-1}. The authors attributed the hydrogen evolution activity of Fe-WO$_x$P/rGO to the synergic effect between high oxygen vacancies of Fe-WO$_x$P and the rGO sheet.[58]

Copper foam-supported Cu$_3$P nanowire arrays (Cu$_3$P NW/CF), Cu$_3$P microsheets on nickel foam and Cu$_3$P nanowires constructed on Cu mesh were fabricated and exhibited Tafel slopes of 67–107 mV dec^{-1} for the hydrogen evolution reaction, suggesting a relatively slow reaction kinetics on the Cu$_3$P catalysts.[59–61] Chen and Yu have carried out DFT calculations and revealed that the Ni heteroatoms exhibited opposite binding ability with H, and could optimize the adsorption state of H* on Cu$_3$P structure. Therefore, doping Cu$_3$P with Ni could be a promising strategy to improve the HER catalytic activity of Cu$_3$P electrocatalysts.[62]

3.3. Metal nitrides

Metal nitrides also act as a class of promising noble-metal-free catalysts for hydrogen evolution reaction. Co$_3$O$_4$ could be directly converted into cobalt nitride (CoN) by using N$_2$ radio frequency (RF) plasma treatment. The obtained CoN nanowires showed a relatively small Tafel slope of 70 mV dec^{-1} and an overpotential of 290 mV at 10 mA cm^{-2}. It can sustain a 30 h operation of hydrogen evolution in KOH.[65] Sasaki and co-workers have synthesized MoN and NiMoN$_x$ nanosheets for HER (Figure 10). The NiMoN$_x$/C catalyst exhibited a small Tafel slope of 35 mV dec^{-1}, a high exchange current of 0.24 mA cm^{-2}, and a low overpotential of 78 mV, suggesting a Tafel-like process as the rate-limiting step in the catalytic hydrogen evolution reaction. In contrast, the MoN/C catalyst had a larger overpotential of 157 mV, a larger Tafel slope of 54.5 mV dec^{-1} and smaller exchange current density of 0.036 mA cm^{-2}.[63] Using a metal–organic framework assisted strategy, the nanosized MoN particles were uniformly dispersed on a highly porous N-doped carbon matrix. The obtained MoN–NC nano-octahedrons presented an extremely large exchange current density of 0.778 mA cm^{-2}, which was like that of Pt/C catalyst (0.78 mA cm^{-2}). The Tafel slope of the MoN–NC nano-octahedrons was 54 mV dec^{-1}, but the overpotential was decreased to 62 mV at 10 mA cm^{-2}.[66] Abghoui and Skulason have investigated the possibility of metal mononitrides for catalyzing the HER through DFT calculations (Figure 11). TaN was assumed as the most promising nitride catalyst for its predicted extremely low onset potential of −0.09 V (vs. RHE). The calculated activation energy and rate of the Tafel reaction on TaN were similar to those of Pt (111) at equilibrium potential. The other nitrides (HfN, MoN and ScN) are also capable to catalyze HER at low overpotentials (< 340 mV).[64]

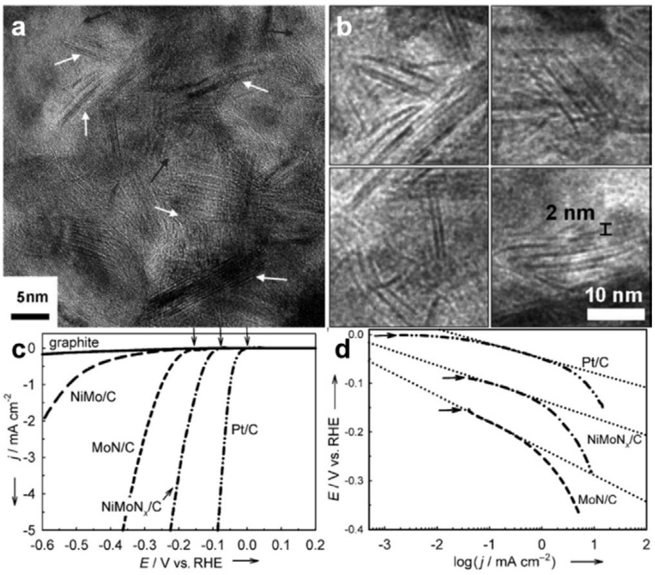

Figure 10. a) High-resolution TEM image and b) magnified images of exfoliated NiMoN$_x$ nanosheets. c) Linear sweep voltammetry curves and d) Tafel plots of MoN, NiMoNx, Pt/C catalyst and graphite in acid media. Reproduced with permission from reference [63]. Copyright 2012, Wiley.

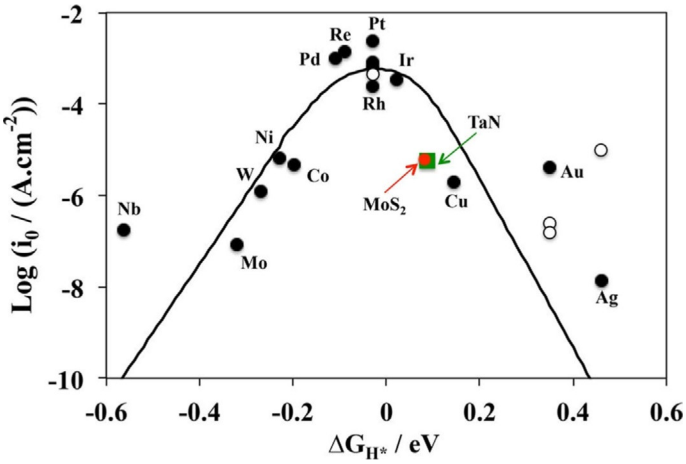

Figure 11. Volcano plot of the HER for various metals, MoS$_2$ and metal nitrides. Reproduced with permission from reference [64]. Copyright 2017, American Chemical Society.

3.4. Metal carbides

Metal carbides, such as Mo_2C and WC, have recently been reported to exhibit catalytic hydrogen evolution activities. Peterson and co-workers have analyzed the correlation between exchange current densities for the HER and hydrogen binding energies on eight mono- and bimetallic carbide electrocatalysts, and a volcano plot was obtained as shown in Figure 12a. These carbides were assumed to behave intermediate activities between Pt and early transition metals. The hydrogen adsorption on the metal carbide surfaces are sensitively decreased along with increasing surface coverage (Figure 12b,c), leading to increased HER activities.[67]

2D layered Ti_2CT_x and Mo_2CT_x (T_x = surface functional groups) MXenes were synthesized by Jaramillo and Vojvodic. The Mo_2CT_x exhibited far higher activity than Ti_2CT_x for hydrogen evolution reaction. The basal planes of Mo_2CT_x were identified as the catalytically active sites for HER, rather than the edge sites.[70] A density functional theory study of hydrogen evolution reactions on cubic MoC has indicated that the MoC [110] surface may possess a high rate for the HER. At low potentials, the adsorption of H atom would compete with N atoms on MoC surfaces except the MoC (111) (Figure 13a). Increasing the Mo/C atom ratio may introduce some carbon vacancies, which will decrease the accumulation of H-adatoms and alleviate hydrogen evolution.[68]

Molybdenum carbides deposited on carbon-based materials were reported to be effective hybrid nano-electrocatalyst for HER. The Mo_2C supported on carbon nanotube presented an overpotential of 63 mV for current density of 1 mA cm^{-2}.[71] Zou, Chen, and Asefa have synthesized Mo_2C nanoparticles embedded in nitrogen-rich (NC) carbon nanolayers. The Tafel slope decreased from 110 mV dec^{-1} of Mo_2C to 60 mV dec^{-1} of Mo_2C@NC catalyst, which also showed a higher exchange current density (0.096 mA cm^{-2}) than that of Mo_2C (0.0012 mA cm^{-2}). The theoretical studies confirmed a synergistic effect between the Mo_2C nanoparticles and the N dopants in Mo_2C@NC catalyst. The neighboring C atoms act as both electron acceptors and donors, suggesting a complex electron-transfer process of $Mo_2C \rightarrow C \rightarrow N$ in Mo_2C@NC catalyst. The C atoms adjacent to N atoms in the carbon layer were identified to be the catalytically active sites responsible for the high activity of the Mo_2C@NC (Figure 13b).[69]

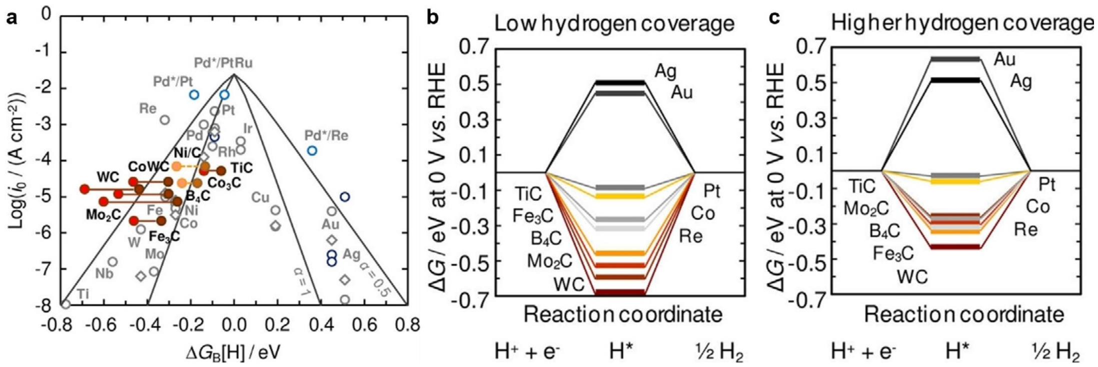

Figure 12. a) Volcano plots for the HER on various transition metals and metal carbides. Free energy diagrams for the electrochemical reduction of H^+ at b) low coverage or c) higher coverage on metal or metal carbide surfaces. Reproduced with permissionfrom from reference [67]. Copyright 2014, American Chemical Society.

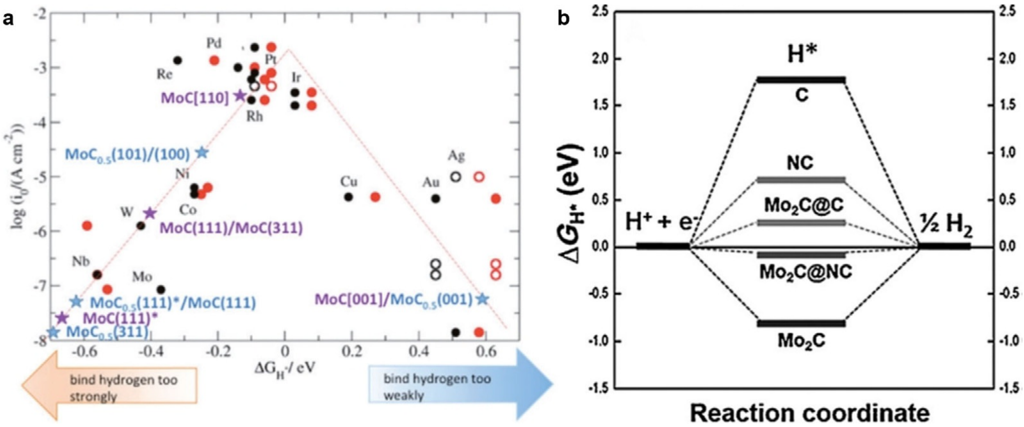

Figure 13. a) Exchange current, log(j_0) versus hydrogen adsorption free energies for hydrogen evolution over different metal surface. Reproduced with permission.[68] Copyright 2018, Royal Society of Chemistry. b) Diagram of calculated free energy for HER on different electrocatalysts. Reproduced with permission from reference [69]. Copyright 2015, Wiley.

An extremely small Mo_2C nanoparticles with sizes smaller than 3 nm encapsulated by 1–3-layer graphene shells showed a small Tafel slope of 41 $mV\,dec^{-1}$ and a very low onset potential of −6 mV for hydrogen evolution. This highly active Mo_2C catalysts gave a large exchange current density of 0.179 $mA\,cm^{-2}$ and a long-term stability of 12 h in acidic solution for HER.[72] The Mo/β-MO_2C hetero-nanosheets only presented a Tafel slope of 70.72 $mV\,dec^{-1}$ and an overpotential of 79 mV at current density of 10 $mA\,cm^{-2}$ for hydrogen evolution.[73]

The P introduced $MoPC_x$/N hybrid catalyst showed a Tafel slope of 69.4 $mV\,dec^{-1}$.[74] Decorating Mo_2C with a sulfur outer shell to form an $Mo_2C@MoS_x$ catalyst, the Tafel slope decreased to 44 $mV\,dec^{-1}$, suggesting a fast water reduction kinetics on the $Mo_2C@MoS_x$ catalyst.[75] A relatively small Tafel slope of about 53 $mV\,dec^{-1}$ was realized on the nanoporous Mo_2C nanowires. This could be attributed to the enriched nanoporosity and large reactive surface of these highly dispersed nanowires.[76]

The tungsten carbides (WC) are less active for HER (Tafel slope, 82 $mV\,dec^{-1}$), but more conductive compared with Mo_2C (Tafel slope, 58 $mV\,dec^{-1}$). Integrating Mo_2C onto WC, the obtained W_xMoC presented the similar Tafel slope (56 $mV\,dec^{-1}$) as that of Mo_2C, suggesting a Volmer–Heyrovsky reaction route for HER. However, the exchange current density was increased from 0.0058 $mA\,cm^{-2}$ for Mo_2C to 0.029 $mA\,cm^{-2}$ for W_xMoC catalysts after electrochemical activation due to partially removal of the surface carbon and change of surface hydrophilicity. In fact, the residual carbon after the activation would also benefit for the catalytic activity.[78] Recently, Chen and Li have prepared tungsten carbide nanoclusters with sizes about 2 nm (Figure 14a), which exhibited a Tafel slope of 49 $mV\,dec^{-1}$, very low overpotential of 51 mV at 10 $mA\,cm^{-2}$ and an extremely high exchange current density of 2.4 $mA\,cm^{-2}$, which was reported to be the highest value among all carbides and W/Mo-based catalysts (Figure 14b,c).[77]

4. Oxygen Evolution Catalysts

Water oxidation (OER: $2H_2O \rightarrow O_2 + 4H^+ + 4\,e-$) into molecular oxygen provides the protons and electrons required for reductive half reactions, for example, the reduction to hydrogen, carbon dioxide reduction into the carbohydrate, and nitrogen reduction into ammonia. Water oxidation is not only the primary step in photosynthesis, but also in renewable energy storage (Figure 15).

There are three well-known OER catalysts available in natural systems or used in industry, the Mn_4 cluster, iridium oxides, and nickel hydroxides used in nature, acidic electrolyzers, and alkaline electrolyzers, respectively. In nature, the Mn_4 cluster is the oxygen evolution center harbored in photosystem system II, in which the aqueous environment is near neutral.[79] Photosynthesis is the primary process that provides the oxygen and biomass on Earth.

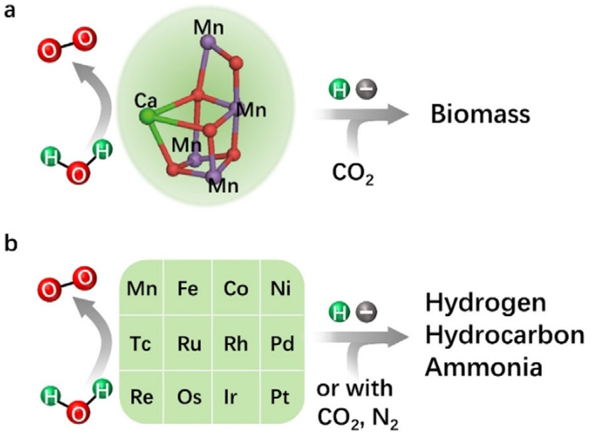

Figure 15. OER in a) natural photosynthesis process and b) artificial electrolysis systems.

In artificial systems, water splitting into hydrogen and oxygen has been successfully used for the production of high-purity hydrogen, but on a limited-scale. In the acidic proton-exchange membrane (PEM) electrolyzer and the alkaline aqueous electrolyzer, the two commercial available water electrolysis technologies, iridium-based metal oxides and nickel-based metal alloys are used as benchmark OER catalysts, respectively.[80,81] The large-scale application of these technologies requires improvement in efficiency, stability, and scalability so that they can compete economically with hydrogen generation from fossil-fuel-based steam reforming method. From the engineering point of review, the electrical resistance of the electrolyte and the bubble are the two significant sources of energy loss in water electrolysis, which can be optimized by advanced engineering technologies. However, from the electrocatalytic

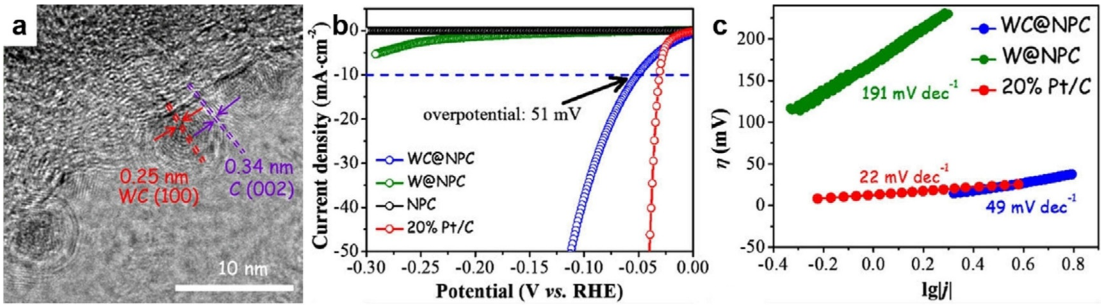

Figure 14. a) HRTEM image of WC/NPC (nanoporous carbon) catalyst. b) Linear sweep voltammetry and c) Tafel plots of different electrocatalysts. Reproduced with permission from reference [77]. Copyright 2017, American Chemical Society.

material point of view, the large overvoltage of the oxygen and hydrogen evolution reaction has been the largest source of energy loss in water electrolysis, especially, the overvoltage (η) required for spin inversion to produce the triplet oxygen, that is, the overpotential for oxygen evolution.[82] Hence, OER electrocatalysts made from earth-abundant elements with long-term stability and low overpotentials are highly desirable and draw great of research interest in recent years.

McCrory et al.[83] proposed the standard protocol for the measurement of the activity, stability, and Faradaic efficiency of the electrocatalysts in acidic and alkaline solution. For comparison, the overpotential is determined at a current density of 10 mA cm^{-2} at 25 °C under 1 atm O_2, which is the approximate current density expected for a 10 % efficiency of a solar water splitting device under 1 sun illumination. Sometimes, the efficiency of the electrolysis is overestimated when the Faradaic efficiency of OER is not 100 % if the substrate is metal and carbon or the catalysts contain low valence state species that are readily oxidized. Therefore, it is crucial to carry out the measurements of Faradaic efficiency for both hydrogen and oxygen using GC measurements, and determine the overpotential after 2 h of constant polarization. This protocol not only allows for the rapid screening and comparing of electrocatalytic performance, but also provides useful data with standard electrochemical procedures for data mining to discover more efficient OER electrocatalysts across a wide untouched chemical space when combined with machine learning.

4.0.1. OER catalysts in alkaline media

In alkaline aqueous water electrolysis, strong base is used as the electrolyte. Potassium hydroxide is the more popular choice than sodium hydroxide owing to its better conductivity. The molar ion conductivities of Na^+, K^+, and OH^- are 0.0501, 0.0735, and 0.1986 S L mol^{-1} cm^{-1}, respectively. Most of the transition metals are stable in alkaline media by forming a metal hydroxide layer. The biggest advantage of alkaline electrolysis under alkaline conditions is the application of the earth-abundant transition metals for use in water oxidation.[81] The biggest challenge of the alkaline water electrolysis is the high resistance coming from the gas bubbles and the ionic transfer. In this case, alkaline-exchange membranes with high conductivity and durability, and efficient and abundant water oxidation catalysts are hot research topics nowadays for alkaline water electrolysis.

4.0.2. OER catalysts in acidic media

The development of acidic water electrolysis owes its success to the availability of high proton conductivity membranes, that is, proton exchange membranes (PEMs). The proton has the highest molar conductivity of 0. 3498 S L mol^{-1} cm^{-1} among all ions. Compared with the alkaline electrolyzer, a PEM with low internal resistance can operate at much higher current densities (>2 A cm^{-2}), with compact system design, low gas crossover and high voltage efficiency, which reduce the operational costs of electrolysis. Besides, the PEM electrolyzer also exhibits a rapid system response, which is of great advantage for the field of fluctuating renewable energies storage, especially for the wind power and the solar power. The corrosive acidic regime provided by the proton exchange membrane (pH ca. 2) requires the use of acidic corrosion-resistance materials both for the setup and the catalysts.[80] Recently, a variety of earth-abundant-element HER catalysts have been reported that work in a large pH range.[84,85] However, there are only a few OER catalysts that contain earth-abundant elements that are acid stable, which hinders the large-scale application of this advanced system. It is reported that terrawatt-level PEM water electrolysis requires over ten years annual production of noble metal iridium (assuming the mass loading of Ir is 0.15 mg cm^{-2}, at current density of 1.4 A cm^{-2} with voltage efficiency of 65 %, Ir annual production of 9 metric tons).[86] For a sustainable hydrogen generation technology, it is necessary to develop the earth-abundant-element, efficient and robust OER catalysts in acidic media, though it is highly challenging.

4.0.3. OER catalysts for neutral media

To date, there is no commercially available, neutral electrolyte water electrolysis system, while, water oxidation in the ecosystem occurs in the cell sap with pH near neutral. Most artificial particulate photocatalysts for overall water splitting are performed at neutral pH.[87] Furthermore, seawater is the most abundance water source on earth and is a naturally available electrolyte with a salt concentration of 3.5 % and pH of around 8; therefore there is remarkable merit to directly use seawater as a proton source. Brine water has been commercially used in the chlor-alkali and chlorate processes for over 100 years—the chloride generation dominated on the anode part at which the dimensionally stable anode (DSA, Ti coated by a mixed oxide of RuO_2 and TiO_2) was used. Direct splitting of seawater into hydrogen and oxygen without chloride generation is a great challenge. So, when we take all the above points into consideration, the development of OER catalysts for neutral media not only sounds attractive, but also has significant meaning as an alternative choice for water splitting to store the renewable energy in the form of hydrogen.

In the following sections, we discuss non-noble-metal-based OER catalysts that are reported to be abundant, efficient, and stable. The mechanism of OER electrocatalysts, the potential application of the OER catalysts in a wide pH range as well as the future research directions will also be presented and discussed.

4.1. Nickel-based OER catalysts

Nickel-based metal alloys are the most popular OER catalysts due to its abundance, low cost, high activity, and easy availability. Nickel has been used as the essential OER catalyst in the commercial alkaline water technology for over 130 years.[88] Until 30 years ago, researchers noticed the importance of impurities in promoting the OER activity, especially the iron impurities in nickel oxide facilitate the oxygen evolution reaction.[89] The effects of iron doping on the OER performance of

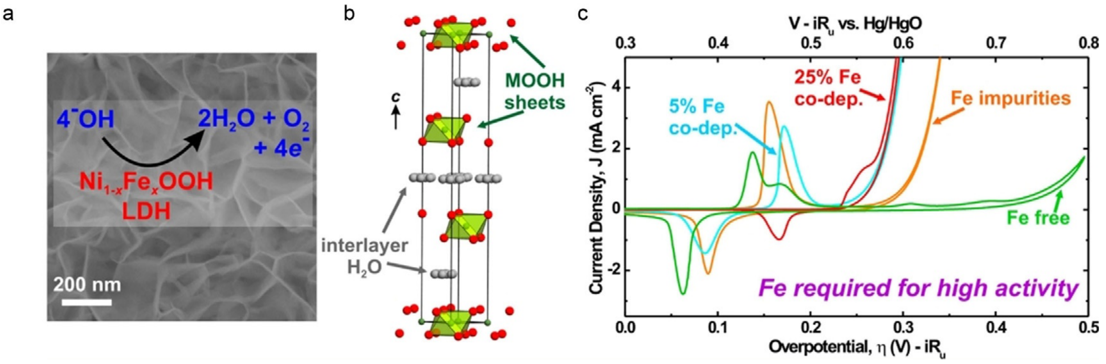

Figure 16. a) Schematic diagram of water oxidation on layered double hydroxide $Ni_{1-x}Fe_xOOH$ in alkaline media. b) Crystal structure NiFe layered double hydroxide (fougerite; ICSD 159700; note that this is the all-Fe analogue) viewed roughly along the 110 direction. c) CV scans of $Ni_{1-x}Fe_{x}(OH)_2$/$Ni_{1-x}Fe_xOOH$ films deposited on IDA electrodes. Currents are not normalized for differences in film thickness, and potential values are not corrected for series resistance. Reproduced with permission from reference [93]. Copyright 2014, American Chemical Society.

nickel oxides have been extensively studies in recent years (Figure 16), including the ratio of Fe:Ni, the changes of Ni^{II}/Ni^{III} redox peak according to the amount of Fe and the reaction center, and so forth.[90,91] Boettcher et al. investigated the OER electrocatalytic properties of ultra-thin metal oxides, such as NiO_x, CoO_x, $Ni_yCo_{1-y}O_x$, $Ni_{0.9}Fe_{0.1}O_x$, IrO_x, MnO_x, and FeO_x. $Ni_{0.9}Fe_{0.1}O_x$ was found to be the most active OER catalyst in 1 M KOH, reaching 10 mA cm^{-2} at an overpotential of 336 mV with a Tafel slope of 30 mV dec^{-1}.[92] They also reported that even an accidental incorporation of iron could enhance the catalytic activity. For example, a freshly deposited NiOOH film increases in activity by over 20-fold during exposure to the electrolyte (KOH) containing trace of Fe. In contrast, Fe-free NiOOH showed very poor electrocatalytic activity.[93] Almost all the reported benchmark catalysts for water oxidation in alkaline condition contain Ni or both Ni and Fe.[94–96]

The electrochemical equilibria of nickel in aqueous solutions is well described in the Pourbaix diagram (Figure 17).[97] Calculated Pourbaix diagrams may be used as guidance for the selection of passivated oxide phases that persist at the aqueous conditions and high potentials. Nickel oxide (NiO_x) is stable only at high pH under positive potentials. In the alkaline electrolysis industry, Raney nickel (NiAl alloy) is used as the anode. During water electrolysis, the Al will partially dissolve into the electrolyte and porous Ni/nickel hydroxides will form as the active OER catalyst layer. Interestingly, it is reported that the addition of a redox-inert metal species could also enhance the water oxidation activity. Stahl et al. reported that an inverse spinel $NiFeAlO_4$ material shows activity exceeding previously reported nickel containing electrocatalyst, including NiO, NiFe (9:1), and $NiFe_2O_4$. It was supposed that the Al^{III} could activate a water molecule for O–O bond formation.[98]

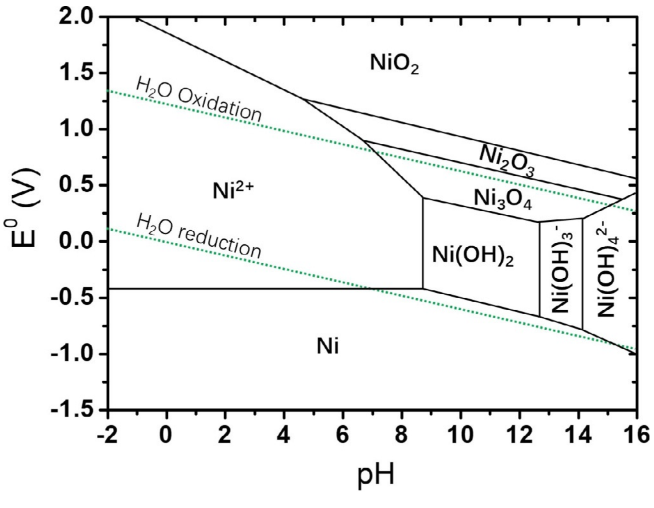

Figure 17. Pourbaix diagram (potential–pH) calculated for the nickel/water system. System also described in reference [97].

4.2. Cobalt-based OER catalysts

Cobalt has been identified as another promising candidate anode catalyst for alkaline water electrolysis, and a number of cobalt-based materials have been developed as non-noble-metal electrocatalysts for OER.[99] The comparisons of different cobalt oxides (CoO_x, Co_3O_4, CoO and ε-Co) with similar sizes, shapes, and the same surface stabilizers provided by the Tilley group show that these nanoparticles present similar OER activity in alkaline conditions.[100] In other work, Zou et al. synthesized a bimetallic ZnCo layered double hydroxide that had a lower overpotential, by about 100 mV, than $Co(OH)_2$ and Co_3O_4. Moreover, the turnover frequency of the synthesized catalyst is >10 times higher than those of $Co(OH)_2$ and Co_3O_4 at the same applied potentials.[101] Co_3O_4 is one of the most important cobalt-based spinel oxides, known to be built around a closed packed array of O^{2-}, with Co^{2+} and Co^{3+} cations occupying part or all of the tetrahedral and octahedral sites, respectively. In recent years, Co_3O_4 has been widely investigated as an essential component in water splitting, supercapacitors, and secondary batteries. The physicochemical properties and OER activity in alkaline media are highly dependent on the composition, structural properties, and oxidation states of the cations.[102]

However, the abundance of cobalt is about one third of that for nickel. Moreover, a large part of cobalt is produced as a by-product of nickel and copper, with annual production less than

10 % of that for nickel. The supply of cobalt seems to have limited elasticity.[103] During the last two years, the price of cobalt witnessed a rapid increase owing to the increased production of electric vehicles. There is a long way to go before cobalt-based OER electrocatalysts can compete with the available nickel-based anodes used in alkaline aqueous water electrolysis, from both an economical and sustainable point of view.

Cobalt oxide (CoO_x) is stable only at high pH under positive potentials, according to the Pourbaix diagram, which shows the redox states and species of the cobalt under different conditions (Figure 18). Nevertheless, Nocera and co-workers reported that in situ generated CoPi, using electrodeposition of Co^{2+} in phosphate buffer solution, was a highly active OER catalyst. The deposited CoPi displayed an overpotential of 410 mV at 1 mA cm^{-2} and a long-term stability owing to its self-healing property (Figure 19).[104] The proposed mechanism of the OER and the self-healing were predicted by Surendranath et al.by using in situ X-ray absorption near-edge structure (XANES) spectroscopy, pH-dependent experiments and ^{18}O isotope labeling experiments. The Co^{III}-centered catalysts undergo oxidation to Co^{IV} under OER potentials, followed by oxygen evolution and relaxation of Co^{IV} into Co^{II}. Here the Co^{II} tends to be oxidized into Co^{III} under anodic potential instead of dissolving into the electrolyte, giving the catalysts functional stability.[105]

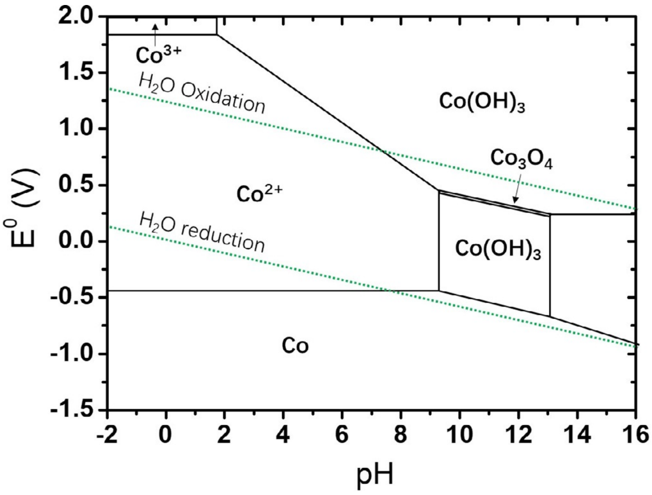

Figure 18. Pourbaix diagram (potential–pH) calculated for the cobalt/water system. System also described in reference [97].

The capability of CoPi working under neutral conditions also triggered intensive research for searching OER catalysts working in natural electrolyte (the seawater and the river water). Nocera's group also reported that the porous CoBi could achieve current density of 100 mA cm^{-2} at an overpotential of 363 mV, which is 79 mV lower than that of CoPi at the same current density. The two catalysts retain excellent activity in buffered natural river water and seawater at neutral pH.[106] Since the report on the efficient and stable OER performance of Co-based OER catalyst under neutral buffered conditions, it prompted numerous other groups to look for more efficient neutral stable OER catalysts. In particular, Hsu et al. reported that transition-metal hexacyanometallates $Co_2[Fe(CN)_6]\cdot n\,H_2O$ demonstrate excellent OER performance in buffered seawater, achieving an extraordinary solar-to hydrogen efficiency of 17.9 % when combined with a single III–V triple-junction solar cell.[107] Mondschein et al., have shown that Co_3O_4 films fabricated by the electrodeposition–annealing method, are capable of sustained OER activity at operationally relevant current densities in strongly acidic solutions. However, the cobalt oxides still readily dissolve in acidic solutions, especially at oxidizing potentials, at rates of approximately 1–100 ng min^{-1}, depending on the pH and applied potential. Additional electrode engineering and corrosion protection strategies may help to decrease the dissolution rate to produce even longer-lasting catalyst films.[108] Interestingly, an acid-compatible Co-based polyoxometalate, with inorganic, anionic, metal-oxide frameworks that can stabilize the cobalt in acid, has shown competitive activity with state-of-the-art iridium oxide (IrO_2) in acid. However, it is not known how the barium cations and the hydrophobic environment provided by the carbon paste influence the activity and the stability.[109]

4.3. Iron-based OER catalysts

Iron is the most abundance transition-metal element on Earth, with the largest annual production among all the metal materials; it is also much cheaper and less toxic compared with

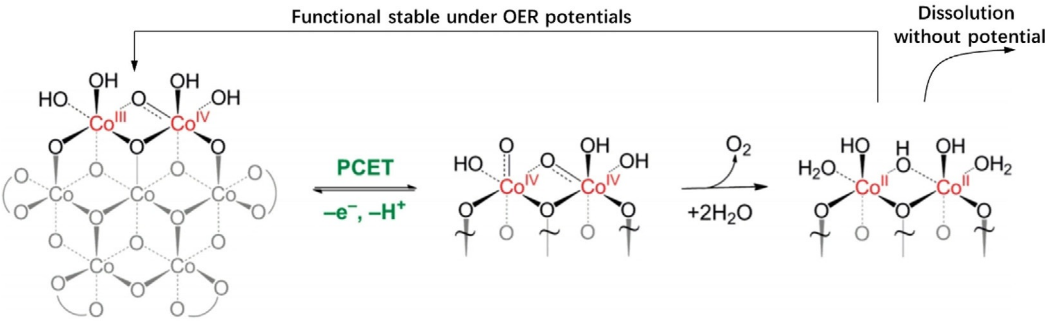

Figure 19. Proposed structure and OER mechanism of CoPi water oxidation electrocatalyst in buffered neutral condition. A PCET equilibrium shows that the generation of the reactive Co^{IV} proceeded by rate-limiting O–O bond-forming and Co^{II}-forming steps. The readily soluble Co^{II} tends to be deoxidized into Co^{III} under OER potentials. Curved lines denote phosphate, or OH terminal or bridging ligands. Reproduced with permission.[105] Copyright 2010, American Chemical Society.

cobalt and nickel. The large-scale application of iron in the energy conversion or storage technologies has great merit. The electrochemical equilibria of iron in aqueous solutions is well described in the Pourbaix diagram (Figure 20). Due to the semiconductor properties of most of the iron oxides, most of them could not be directly used as electrocatalysts as bulk form. Somorjai et al. reported that an iron oxide electrode (α-Fe_2O_3) with absorption wavelengths longer than 500 nm has excellent long-term stability in photoelectrocatalytic water splitting. However, the very short photo-induced hole lifetime hinders its efficiency (0.05 %), which is a major obstacle for its application.[110] By doping Fe_2O_3 with silicon, Gratzel et al. were able to increase the photoresponse of nanocrystalline α-Fe_2O_3 films, achieving a solar-to-chemical conversion efficiency of 2.1 % when combined with a tandem device.[111]

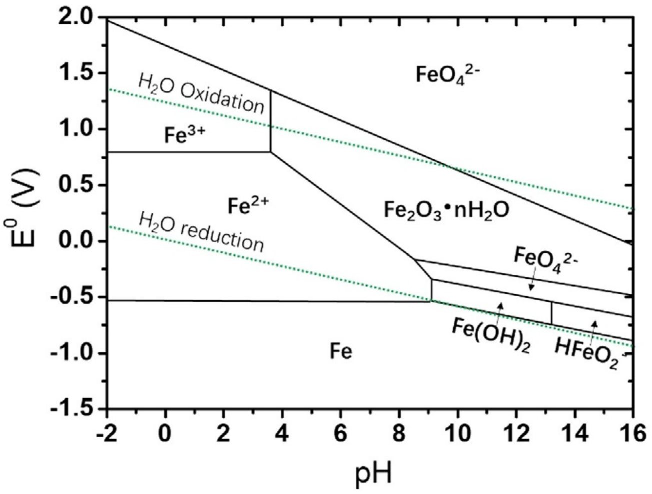

Figure 20. Pourbaix diagram (potential–pH) calculated for the iron/water system. System also described in reference [97].

Iron-based materials have been suggested to be potential electrocatalysts for OER, owing to the fact that most of the efficient Co- or Ni-based OER catalysts contain non-negligible mounts of Fe. However, the water oxidation performance of the pure γ-FeOOH was reported to be very poor.[112,113] Compared with cobalt and nickel, iron-based electrocatalytic water oxidation materials have not been broadly investigated. On the other hand, the particular function of iron as an incorporated dopant/impurity into the Ni-/Co-based OER catalysts, which dramatically improving their water oxidation performance, has attracted much research interest. Iron-based materials have also been widely employed as cocatalysts combined with semiconductor absorbers for photoelectrochemical water splitting. Significantly enhanced photocurrent and stability for the $BiVO_4$ were achieved after photodeposition of FeOOH on $BiVO_4$.[114] A ferrihydrite, denoted as $Fe_5HO_8{\cdot}3\,H_2O$, is also reported to function as a charge storage capacitor layer and a corrosion protective layer between the metal nitride semiconductor photoanodes and the Co_3O_4 electrocatalysts layer or the molecular catalysts.[115,116]

4.4. Manganese-based OER catalyst

Manganese is the 12th most abundant element in the Earth's crust. It is also the 4th mostly used metal material, following iron, aluminum, and copper, in industry. Manganese can have many oxidation states (+2, +3, +4, +5, +6, +7) in over 30 different crystal structures, and over 450 valid minerals contain manganese.[117] Manganese is the core element in water oxidation catalyst found in all cyanobacteria, algae, and plants. This catalyst is housed in photosystem II in the form of a Mn–Ca cluster. Water oxidation in the photosynthesis system provides the necessary electrons and protons for the biomass formation and oxygen for the Earth life, regarded as the fundamental process of the Earth's ecosystem.[79] Water oxidation here is carried out in a series of proton-coupled electron transfer (PCET) noted as the Kok cycle (Figure 21).[118] Without PCET, charge would build up on the catalysts, hindering the second, third, and fourth oxidation steps.[119] Such PCET processes have been reported for artificial oxygen evolution systems.[120,121]

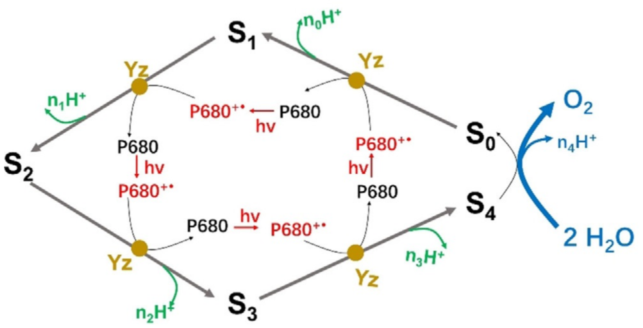

Figure 21. Kok cycle of oxidative water splitting in PSII. Reproduced with permission from reference [118]. Copyright 2012, Elsevier.

Manganese-based electrocatalysts have been extensively studied in artificial water splitting systems.[79] Meng et al. have shown that the overpotential of manganese oxide with different structures at 10 mA cm^{-2} displayed in the order of α-MnO_2 > amorphous oxide > β-MnO_2 > δ-MnO_2 in 0.1 M KOH at 10 mA cm^2.[122] α-MnO_2 and δ-MnO_2 display tunneled and layered structures that can host various cations and molecules, exhibiting unique adsorptive properties that is beneficial for various different electrochemical reactions.

Manganese oxide (MnO_x) is stable at a full pH range under suitable positive potentials, according to the Pourbaix diagram (Figure 22). The activity and stability of manganese oxides in neutral and acidic condition have drawn lots of attention. Takashima et al. have reported that an absorption band with a peak at around 510 nm was generated during the OER cycle by an Mn oxide electrocatalyst. In situ water oxidation measurements showed that the absorption peak is due to the d–d transition of surface-associated Mn^{3+}. The Mn^{3+} is supposed to be formed by electron injection from H_2O to anode-polarized MnO_2, which is regarded as the precursor for the OER. While Mn^{3+} is unstable at pH < 9 due to charge disproportionation

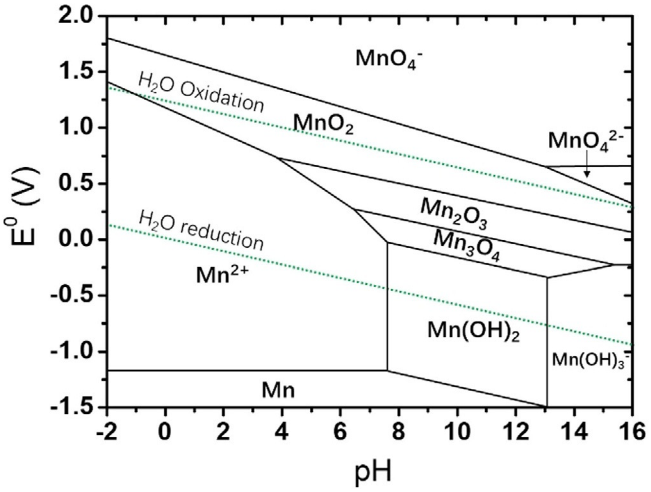

Figure 22. Pourbaix diagram (potential–pH) calculated for the manganese/water system. System also described in reference [97].

($2Mn^{3+} \rightarrow Mn^{2+} + Mn^{4+}$), it could be stabilized by charge comproportionation (CC) ($Mn^{2+} + MnO_2 \rightarrow Mn^{3+}$) under alkaline conditions. Thus, the sharp decrease in the catalytic activity of MnO_2 at $pH < 9$ is supposed to be the inherent instability of Mn^{3+}. At $pH > 9$, the Mn^{3+} species is supposed to be stable enough to participate in OER.[123,124]

Huynh et al. studied water oxidation using MnO_x films under acidic conditions. They reported that the self-healing nature of MnO_x could partially offset the degradation of manganese during oxygen evolution in highly acidic electrolytes at current density of 10 uA cm^{-2}. In other words, it was supposed that the films would maintain their OER stability through self-repair by deposition of the dissolved manganese at potentials below those required for OER.[125] However, the water oxidation activity of the electrodeposited MnO_x films can be made two orders of magnitude higher by changing the deposition protocol from a constant anodic potential to a voltage cycling routine, reaching 1 mA cm^{-2} at 600 mV cm^{-2}. Frydendal et al. reported a strategy by selectively terminating undercoordinated sites on MnO_2 with titanium determined by DFT calculations. The sputter-deposited thin films of pure MnO_2 and Ti-doped MnO_2 were tested in 0.05 M H_2SO_4. The ICP-MS and EQCM measurements showed that the mass losses could be moderately decreased by incorporating Ti into the catalyst, with only a small drop in catalytic activity toward OER. Therefore, the experimental results suggested that a more optimal balance between stability and activity could be achieved by engineering the surface properties of MnO_2.[126]

4.5. The perovskite-type OER catalysts

Transition-metal-based perovskite oxides have the general formula ABO_3, in which smaller transition-metal ions on the B-site reside in corner-sharing octahedra of O^{2-} anions, and larger alkali metal or rare-earth A-site cations have 12-fold coordination with O^{2-}. Owing to the flexible components and electronic structure, the perovskite materials found applications in various fields.[127] The first work on perovskite-based OER catalyst dates back to the 1970s.[128,129] Since then, extensive theoretical and experimental studies have been reported. Perovskites are typically synthesized by high temperature solid-state reactions with stoichiometric amounts of solid starting materials by grinding in an agate mortar; they show good intrinsic OER activity but low surface area (typically $< 4\ m^2 g^{-1}$). Suntivich et al. et al. described a novel method for rational design of perovskite materials for the oxygen evolution reaction.[130] They discovered a quaternary perovskite-structure, $Ba_{0.5}Sr_{0.5}Co_{0.8}Fe_{0.2}O_3$ (BSCF), that works even better than iridium oxide. They conducted a systematic theoretical investigation on several types of perovskites and deduced the number of occupied d orbital states of a specific symmetry (e_g) of the active metal, which can be used as a descriptor for the catalyst performance (Figure 23 a). Subsequent synthesis and electrochemical performance tests revealed this descriptor to be effective and correct.

Moreover, Hong and co-workers have provided physicochemical parameters that are influence the catalytic activity of the perovskite-based OER catalysts by statistically analyzing 101 intrinsic OER activities of 51 perovskites from previous literature across a wide range of chemistries (Figure 23 b).[131] They confirmed that the number of d electrons, charge-transfer energy (covalency), and optimality of e_g occupancy play the important roles on the OER activity, and additionally the structural factors, such as M-O-M bond angle, and tolerance factor are relevant as well. This work opens up unprecedented opportunities to use machine-learning methods to predict the catalytic activity of new OER catalysts.

Low surface area hinders the transfer of high intrinsic activity of the perovskite-based materials to a real electrolysis system. Novel methods in preparation of catalysts with improved surface area, and conductivity are critical important.[132] A single-step gas-phase process, based on a liquid-fed flame spray synthesis (FSS) technique has been developed to synthesize crystalline perovskite nanopowders with specific surface area of 12–48 m^2 g^{-1}.[133] Operando XAS electrochemical measurements of the $Ba_{0.5}Sr_{0.5}Co_{0.8}Fe_{0.2}O_{3-\delta}$ nanocatalysts reveal substantial and irreversible changes in the electronic structure and local atomic environment at potentials at which the OER occurs, that is, allowing a dynamic self-reconstruction of the material's surface during OER by forming a metal oxy(hydroxide) active layer. The outstanding OER performance has also been verified by operating the nano-sized $Ba_{0.5}Sr_{0.5}Co_{0.8}Fe_{0.2}O_{3-\delta}$ as the anode material in an alkaline membrane water electrolysis cell.[134] The ability of metal oxides to undergo lattice oxygen evolution reactions (LOERs, that is, oxidation of lattice oxygen) was regarded as the origin of catalyst self-reconstruction (Figure 24). In addition it has been demonstrated by basic thermodynamic arguments that the thermodynamic instability of the oxygen anion in the metal oxide lattice is irrespective of the pH value, especially at potentials above the oxygen evolution equilibrium potential. Also the thermodynamic instability of the lattice oxygen could be closely related to the structural changes, the dissolution of the metal oxide and the onset of OER.[135]

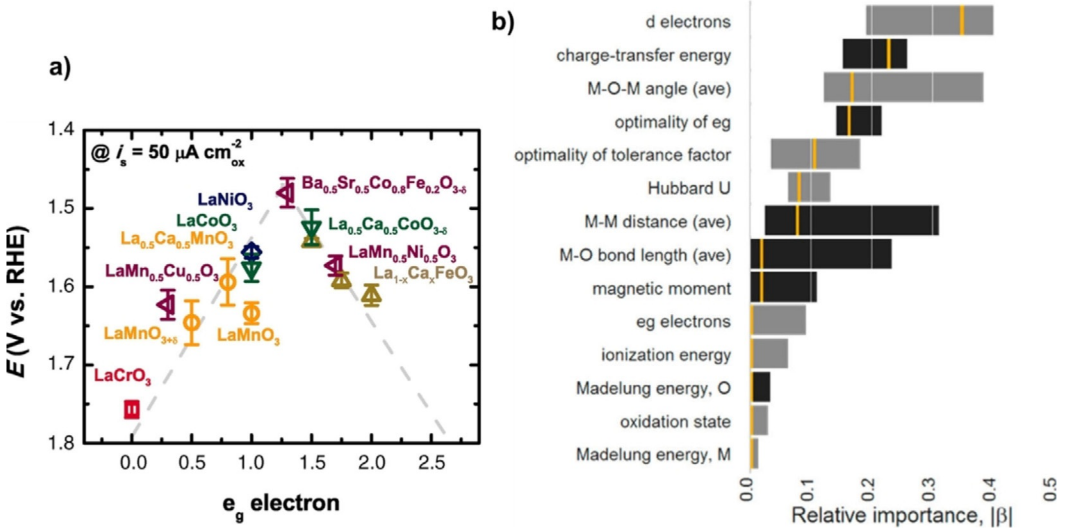

Figure 23. Descriptors for catalyst performance. a) The relation between the OER catalytic activity and the occupation of d states with e_g symmetry. The occupancy of the e_g-symmetry electron is regarded as a good descriptor for the oxygen evolution reaction over metal oxide catalysts. The activities of the catalysts were defined by the overpotentials at 50 μA cm^{-2}. Reproduced with permission from reference [130]. Copyright 2011, AAAS. b) Relative importance of descriptors variables for the penalized regression models used for the statistical evaluation and predication of the OER activity of perovskite-based OER catalysts. Reproduced with permission from reference [131]. Copyright 2015, American Chemical Society.

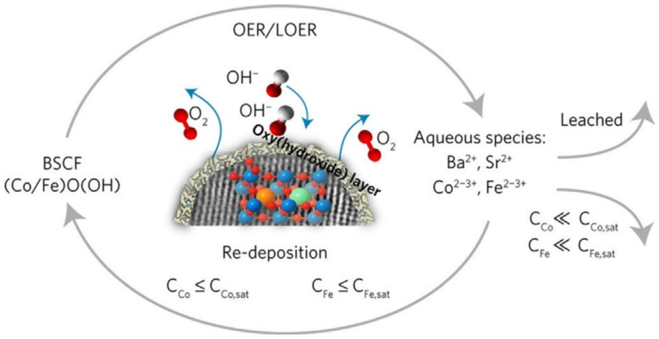

Figure 24. OER/LOER and dissolution/re-deposition mechanism leading to the formation of a self-assembled active surface layer, rich in CoO(OH) and FeO(OH). The LOER process leads to cation dissolution. Ba^{2+} and Sr^{2+} cations are highly soluble and thus, they can easily leach out from the perovskite structure. LOER also triggers dissolution of Co and Fe cations. However, being rather insoluble species, Co and Fe re-deposition on the catalyst surface can take place, especially when near the electrode surface the cation concentration (due to the initial dissolution) becomes significant. Furthermore, the lattice oxygen consumed by the LOER can be replenished by OH$^-$ from the electrolyte. Therefore, a stable dynamic cycle is established, permitting the coexistence of a self-assembled active surface layer with the original BSCF perovskite structure.[134] Reproduced with permission from reference [93]. Copyright 2017, Nature Publishing.

4.6. OER catalysts in photoelectrocatalysis and photocatalysis systems

Integrated photoelectrochemical (PEC) water splitting and particulate photocatalytic water splitting technologies are two major direct ways to store solar energy in the form of chemical energy. The assessments of the cost, efficiency, and viability of such devices are available in the recent literature.[136] In this section, the difference of the water oxidation catalysts in the electrocatalytic water splitting and the photo(electro)catalytic water splitting systems will be discussed. The same points are that all these systems require the catalysts with high activity, stability, and scalability. However, different to the electrochemical water splitting system, in photo(electro)catalytic water splitting system, if the catalysts are directly deposited on the surface of the photon absorber materials, it would result in large optical light absorption losses due to the absorption, scattering, and reflection of the catalysts. So, the OER catalysts for photoelectrocatalysis and photocatalysis technologies requires less effect in the light absorption to the absorber. There are five ways to reach such prerequisite (Figure 25). In a realistic catalytic system, one or several catalyst loading technologies will be used for a better light absorption management. Sometimes, the catalyst may also act as a protective layer to prevent the corrosion of the absorber, or an antireflection layer to reduce the light reflection. Catalysts with high extinction coefficient in the visible-light region tend to be used in the thin layer form or special architectures, such as PtO$_x$, IrO$_x$, and Co$_3$O$_4$. For those with a relative low extinction coefficient in the visible-light region, a relatively thick catalyst layer is used for long lifetime, such as the CoPi, or Ni- and Co-based layered double hydroxides. "Transparent" catalyst layers were first generated by Heller et al. by deposition of small amount of catalysts in porous morphologies on InP electrodes.[137] Other materials with relative low OER catalytic performance have been also reported. For example, transparent TiO$_x$,[138] ITO,[139,140] and so forth, which are usually combined with more active electrocatalysts to improve the OER properties. They can serve as the interactive layer between the electrocatalyst and the semiconductor to reduce the charge transfer resistance, or as a passivation layer to protect the absorber.

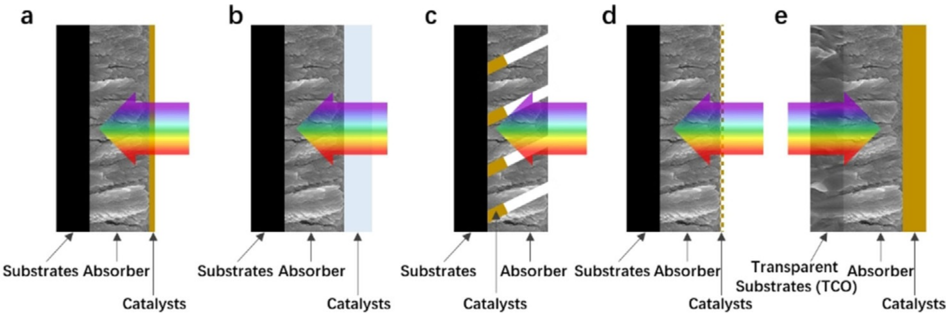

Figure 25. Electrocatalysts design principles of photo(electro)-electrocatalysis systems. a) Thin catalyst layer, b) transparent thick catalyst layer, c), d) catalysts with special architectures, e) transparent substrates with back illumination. System also described in reference [141].

5. Support Materials for OER and HER Catalysts

In this section we highlight the importance in selection of an appropriate substrate for both fundamental study and practical application of the electrochemically active materials. Usage of appropriate support materials could not only help to reduce the loading amount of the noble metals or provide the potential synergetic effect to the target reaction, but also help to prolong the lifetime of the electrolyzer.

5.1. Substrate for fundamental study

In most cases, to accurately evaluate the electrochemically active materials, a chemical inert substrate with appropriate conductivity that exhibits no electrochemical activity under test condition is preferred. Thus, all the electrochemical features can be attributed to the investigated materials. Benck and co-workers proposed an experimental methodology to evaluate the electrochemical features of the potential substrate. They have investigated the inert potential window of seven most popular substrate materials for electrochemical and photo-electrochemical experiments in acidic, neutral, and basic electrolyte, including three transparent conducting oxides (ITO: indium tin oxide; FTO fluorine-doped tin oxide; AZO: aluminum-doped zinc oxide) and four opaque conductors [Au, SS304 (stainless steel 304), GC (glassy carbon), and HOPG (highly oriented pyrolytic graphite)].[142] It is an important preliminary step to evaluate the electrochemical properties of the substrate prior to the catalysts evaluation.

5.2. Support materials for HER

Carbon and metal-based materials with high conductivity are commonly used cathode support materials. In alkaline condition, the most common support/active materials used for the hydrogen evolution reaction are stainless steel and Ni-based alloys due to its low cost and acceptable lifetime.[143] In acidic condition, carbon-based materials are commonly used due to its high acid tolerance and high surface area (e.g., Vulcan XC-72, 235 $m^2 g^{-1}$). Platinum on carbon, denoted as Pt/C, is a form of supported platinum catalyst.

Recent advances in creating supported cathode catalysts have been based on the development of the carbon nanotubes, graphene and other two-dimensional (2D) materials.[144] The 2D materials exhibit excellent electronic and mechanical properties, providing new opportunities in industrial application as active or support materials, for example, the graphene shells encapsulating metal particles,[145,146] metal nanoparticles embedded in porous carbons,[147] and composites of the metal chalcogenides/phosphides/nitride/carbides and carbon materials.[148–151] Furthermore, such 2D crystal structures or composites provide great opportunities in characterization or visualization of the active sites by means of high-resolution transmission electron microscopy and scanning tunneling microscopy.

5.3. Support materials for OER

Molybdenum- and tungsten-containing alloys or steels with good corrosion resistance in concentrated lye solution, high temperature resistance, and good anodic polarization have been used as the anodic support materials in alkaline electrolyte. The electrode could maintain its activity for several years to decades. Compared with the support materials used under alkaline conditions, the anodic support materials face more serious corrosion condition. In addition, the lack of stable and economic supporting materials hampers the development of hydrogen generation through PEM water splitting technology.[152] Carbon-based materials are not sufficiently stable under the harsh oxidizing conditions of the OER, especially for long-time electrolysis tests, which could lead to active particle detachment. Commonly used supports are based on titanium and its oxides as well as conductive transparent oxides, such as FTO and ATO (antimony-tin oxide). Han et al.[52] conducted systematic studies on a number of commercial and synthesized oxide materials as OER catalyst supports (e.g. TiO_x, TiC, SiC-Si, SnO_2, FTO, ATO, PbO_2, MoO_3, WO_3), in which their conductivity and stability under OER condition were compared. Finally, they identified commercial ATO as a promising candidate support material among all the investigated materials under the highly oxidative OER potentials and acidic condition.

6. Conclusions and Perspectives

In summary, recent research progress and trends show that it is possible to develop efficient and robust HER and OER catalysts from earth-abundant elements of first-row transition metals for the replacement of IrO_x and Pt for water electrolysis, though the efficiency and stability are still somewhat problematic. More efforts are needed in searching for more efficient and stable electrocatalysts for water splitting. For the future development, various strategies may be applied to search for cheap, robust, and efficient HER and OER catalysts. Screening and predication of new functional materials by advanced theoretical calculations is necessary to avoid time-consuming trial-and-error experimental methods. Development of self-repairing or self-healing methods is also highly important to solve the stability problems of the current existing many highly active but unstable HER and OER electrocatalysts.

Coupling cheap, robust, and efficient water electrolyzers with renewable energies, such as wind or solar electricity, is the most promising way to produce renewable H_2. Especially as currently the price of the PV electricity has dropped dramatically, and it can be envisioned that PV electricity may be the cheapest electricity among all of the current electricity generation technologies. Simple calculations show the advance of such PV-E technology for H_2 production. Current commercial crystalline Si-PV has a solar-to-electricity conversion efficiency more than 20%. Assuming that the electricity-to-H_2 efficiency is about 60%, this already gives a solar-to-hydrogen (STH) efficiency of more than 12%. Importantly, PV and water electrolyzers are matured technologies. None of the other existing technologies, such as photocatalytic water splitting and photoelectrochemical water splitting, can compete with PV-E in terms of efficiency and durability. As a Chinese proverb says: “It doesn’t matter whether the cat is black or white, as long as it catches mice”, the PV-E technology is the only foreseeable near future technology for large scale production of H_2 with renewable solar energy.

Acknowledgements

This work was supported by the National Key R&D Program of China (No. 2017YFA0204804), the National Natural Science Foundation of China (No. 21761142018, 21401189 and 21473189) and the 973 National Basic Research Program of the Ministry of Science and Technology (No. 2014CB239401).

Conflict of interest

The authors declare no conflict of interest.

Keywords: earth-abundant element catalysts · electrocatalysts · renewable energy · transition metals · water splitting

[1] N. S. Lewis, D. G. Nocera, *Proc. Natl. Acad. Sci. USA* **2006**, *103*, 15729–15735.

[2] C. Song, *Catal. Today* **2006**, *115*, 2–32.

[3] M. Dincă, Y. Surendranath, D. G. Nocera, *Proc. Natl. Acad. Sci. USA* **2010**, *107*, 10337–10341.

[4] M. Conte, F. D. Mario, A. Iacobazzi, A. Mattucci, A. Moreno, M. Ronchetti, *Energies* **2009**, *2*, 150–179.

[5] A. J. Bard, M. A. Fox, *Acc. Chem. Res.* **1995**, *28*, 141–145.

[6] X. Li, X. Hao, A. Abudulaa, G. Guan, *J. Mater. Chem. A* **2016**, *4*, 11973.

[7] R. D. L. Smith, M. S. Prévot, R. D. Fagan, S. Trudel, C. P. Berlinguette, *J. Am. Chem. Soc.* **2013**, *135*, 11580–11586.

[8] S. Anantharaj, S. R. Ede, K. Karthick, S. S. Sankar, K. Sangeetha, P. E. Karthikc, S. Kundu, *Energy Environ. Sci.* **2018**, *11*, 744.

[9] A. B. Laursen, A. S. Varela, F. Dionigi, H. Fanchiu, C. Miller, O. L. Trinhammer, J. Rossmeisl, S. Dahl, *J. Chem. Educ.* **2012**, *89*, 1595–1599.

[10] J. Greeley, T. F. Jaramillo, J. Bonde, I. B. Chorkendorff, J. K. Norskov, *Nat. Mater.* **2006**, *5*, 909–913.

[11] S. A. Vilekar, I. Fishtik, R. Datta, *J. Electrochem. Soc.* **2010**, *157*, B1040–B1050.

[12] E. Skúlason, V. Tripkovic, M. E. Björketun, S. Gudmundsdo’ttir, G. Karlberg, J. Rossmeisl, T. Bligaard, H. Jo’nsson, J. K. Nørskov, *J. Phys. Chem. C* **2010**, *114*, 18182–18197.

[13] B. Owens-Baird, Y. V. Kolen’ko, K. Kovnir, *Chem. Eur. J.* **2018**, *24*, 7298–7311.

[14] T. Heine, *Acc. Chem. Res.* **2015**, *48*, 65–72.

[15] B. Hinnemann, P. G. Moses, J. Bonde, K. P. Jørgensen, J. H. Nielsen, S. Horch, I. Chorkendorff, J. K. Nørskov, *J. Am. Chem. Soc.* **2005**, *127*, 5308–5309.

[16] T. F. Jaramillo, K. P. Jørgensen, J. Bonde, J. H. Nielsen, S. Horch, I. Chorkendorff, *Science* **2007**, *317*, 100–102.

[17] J. Kibsgaard, Z. Chen, B. N. Reinecke, T. F. Jaramillo, *Nat. Mater.* **2012**, *11*, 963–969.

[18] M. A. Lukowski, A. S. Daniel, F. Meng, A. Forticaux, L. Li, S. Jin, *J. Am. Chem. Soc.* **2013**, *135*, 10274–10277.

[19] C. Ling, Y. Ouyang, L. Shi, S. Yuan, Q. Chen, J. Wang, *ACS Catal.* **2017**, *7*, 5097–5102.

[20] D. Voiry, M. Salehi, R. Silva, T. Fujita, M. Chen, T. Asefa, V. B. Shenoy, G. Eda, M. Chhowalla, *Nano Lett.* **2013**, *13*, 6222–6227.

[21] T. Kosmala, H. C. Diaz, H.-P. Komsa, Y. Ma, A. V. Krasheninnikov, M. Batzill, S. Agnoli, *Adv. Energy Mater.* **2018**, *8*, 1800031.

[22] Z. Chen, D. Cummins, B. N. Reinecke, E. Clark, M. K. Sunkara, T. F. Jaramillo, *Nano Lett.* **2011**, *11*, 4168–4175.

[23] Y. H. Chang, C. T. Lin, T. Y. Chen, C. L. Hsu, Y. H. Lee, W. Zhang, K. H. Wei, L. J. Li, *Adv. Mater.* **2013**, *25*, 756–760.

[24] D. J. Li, U. N. Maiti, J. Lim, D. S. Choi, W. J. Lee, Y. Oh, G. Y. Lee, S. O. Kim, *Nano Lett.* **2014**, *14*, 1228–1233.

[25] Z. Chen, K. Leng, X. Zhao, S. Malkhandi, W. Tang, B. Tian, L. Dong, L. Zheng, M. Lin, B. S. Yeo, K. P. Loh, *Nat. Commun.* **2017**, *8*, 14548.

[26] C. Bae, T. A. Ho, H. Kim, S. Lee, S. Lim, M. Kim, H. Yoo, J. M. Montero-Moreno, J. H. Park, H. Shin, *Sci. Adv.* **2017**, *3*, e1602215.

[27] D. Kong, H. Wang, J. J. Cha, M. Pasta, K. J. Koski, J. Yao, Y. Cui, *Nano Lett.* **2013**, *13*, 1341–1347.

[28] Y. Nakayasu, Y. Yasui, R. Taniki, K. Oizumi, H. Kobayashi, N. Nagamura, T. Tomai, I. Honma, *ACS Sustainable Chem. Eng.* **2018**, *6*, 11502–11510.

[29] D. Voiry, H. Yamaguchi, J. Li, R. Silva, D. C. Alves, T. Fujita, M. Chen, T. Asefa, V. B. Shenoy, G. Eda, M. Chhowalla, *Nat. Mater.* **2013**, *12*, 850–855.

[30] S. M. Tan, M. Pumera, *ACS Appl. Mater. Interfaces* **2016**, *8*, 3948–3957.

[31] H. Wang, D. Kong, P. Johanes, J. J. Cha, G. Zheng, N. K. Yan, Y. Cui, *Nano Lett.* **2013**, *13*, 3426–3433.

[32] Y. Sun, X. Zhang, B. Mao, M. Cao, *Chem. Commun.* **2016**, *52*, 14266–14269.

[33] K. Liang, Y. Yan, L. Guo, K. Marcus, Z. Li, L. Zhou, Y. Li, R. Ye, N. Orlovskaya, Y.-H. Sohn, Y. Yang, *ACS Energy Lett.* **2017**, *2*, 1315–1320.

[34] D. A. Henckel, O. Lenz, B. M. Cossairt, *ACS Catal.* **2017**, *7*, 2815–2820.

[35] D. Kong, J. J. Cha, H. Wang, H. R. Lee, Y. Cui, *Energy Environ. Sci.* **2013**, *6*, 3553.

[36] M. Gong, W. Zhou, M.-C. Tsai, J. Zhou, M. Guan, M.-C. Lin, B. Zhang, Y. Hu, D.-Y. Wang, J. Yang, S. J. Pennycook, B.-J. Hwang, H. Dai, *Nat. Commun.* **2014**, *5*, 4695.

[37] X. Zheng, L. Peng, L. Li, N. Yang, Y. Yang, J. Li, J. Wang, Z. Wei, *Chem. Sci.* **2018**, *9*, 1822.

[38] D. Kong, H. Wang, Z. Lu, Y. Cui, *J. Am. Chem. Soc.* **2014**, *136*, 4897–4900.

[39] B. E. Conway, B. V. Tilak, *Electrochim. Acta* **2002**, *47*, 3571–3594.

[40] Z. Fang, L. Peng, Y. Qian, X. Zhang, Y. Xie, J. J. Cha, G. Yu, *J. Am. Chem. Soc.* **2018**, *140*, 5241–5247.

[41] B. Yu, F. Qi, Y. Chen, X. Wang, B. Zheng, W. Zhang, Y. Li, L. C. Zhang, *ACS Appl. Mater. Interfaces* **2017**, *9*, 30703–30710.

[42] C. Di Giovanni, W.-A. Wang, S. Nowak, J.-M. Grenèche, H. Lecoq, L. Mouton, M. Giraud, C. D. Tard, *ACS Catal.* **2014**, *4*, 681–687.

[43] D. Jasion, J. M. Barforoush, Q. Qiao, Y. Zhu, S. Ren, K. C. Leonard, *ACS Catal.* **2015**, *5*, 6653–6657.

[44] R. Miao, B. Dutta, S. Sahoo, J. He, W. Zhong, S. A. Cetegen, T. Jiang, S. P. Alpay, S. L. Suib, *J. Am. Chem. Soc.* **2017**, *139*, 13604–13607.

[45] Y. Chen, J. Zhang, P. Guo, H. Liu, Z. Wang, M. Liu, T. Zhang, S. Wang, Y. Zhou, X. Lu, J. Zhang, *ACS Appl. Mater. Interfaces* **2018**, *10*, 27787–27794.

[46] X. Xu, Y. Ge, M. Wang, Z. Zhang, P. Dong, R. Baines, M. Ye, J. Shen, *ACS Appl. Mater. Interfaces* **2016**, *8*, 18036–18042.

[47] P. Liu, J. A. Rodriguez, *J. Am. Chem. Soc.* **2005**, *127*, 14871–14878.

[48] E. J. Popczun, J. R. McKone, C. G. Read, A. J. Biacchi, A. M. Wiltrout, N. S. Lewis, R. E. Schaak, *J. Am. Chem. Soc.* **2013**, *135*, 9267–9270.

[49] A. B. Laursen, K. R. Patraju, M. J. Whitaker, M. Retuerto, T. Sarkar, N. Yao, K. V. Ramanujachary, M. Greenblatt, G. C. Dismukes, *Energy Environ. Sci.* **2015**, *8*, 1027–1034.

[50] J. Xu, T. Liu, J. Li, B. Li, Y. Liu, B. Zhang, D. Xiong, I. Amorim, W. Li, L. Liu, *Energy Environ. Sci.* **2018**.

[51] P. Xiao, M. A. Sk, L. Thia, X. Ge, R. J. Lim, J.-Y. Wang, K. H. Lim, X. Wang, *Energy Environ. Sci.* **2014**, *7*, 2624–2629.

[52] X. Zhang, X. Yu, L. Zhang, F. Zhou, Y. Liang, R. Wang, *Adv. Funct. Mater.* **2018**, *28*, 1706523.

[53] Z. Pu, Q. Liu, A. M. Asiri, X. Sun, *ACS Appl. Mater. Interfaces* **2014**, *6*, 21874–21879.

[54] J. M. McEnaney, J. C. Crompton, J. F. Callejas, E. J. Popczun, C. G. Read, N. S. Lewis, R. E. Schaak, *Chem. Commun.* **2014**, *50*, 11026–11028.

[55] Z. Xing, Q. Liu, A. M. Asiri, X. Sun, *ACS Catal.* **2015**, *5*, 145–149.

[56] X. Wang, Y. Xu, H. Rao, W. Xu, H. Chen, W. Zhang, D. Kuang, C.-Y. Su, *Energy Environ. Sci.* **2016**, *9*, 1468–1475.

[57] B. Weng, C. R. Grice, W. Meng, L. Guan, F. Xu, Y. Yu, C. Wang, D. Zhao, Y. Yan, *ACS Energy Lett.* **2018**, *3*, 1434–1442.

[58] T. H. Wondimu, G.-C. Chen, D. M. Kabtamu, H.-Y. Chen, A. W. Bayeh, H.-C. Huang, C. H. Wang, *Int. J. Hydrogen Energy* **2018**, *43*, 6481–6490.

[59] J. Hao, W. Yang, Z. Huang, C. Zhang, *Adv. Mater. Interfaces* **2016**, *3*, 1600236.

[60] J. Tian, Q. Liu, N. Cheng, A. M. Asiri, X. Sun, *Angew. Chem. Int. Ed.* **2014**, *53*, 9577–9581; *Angew. Chem.* **2014**, *126*, 9731–9735.

[61] H. Wang, T. Zhou, P. Li, Z. Cao, W. Xi, Y. Zhao, Y. Ding, *ACS Sustainable Chem. Eng.* **2018**, *6*, 380–388.

[62] Z. Zhang, G. Yu, H. Li, J. Liu, X. Huang, W. Chen, *Phys. Chem. Chem. Phys.* **2018**, *20*, 10407–10417.

[63] W. F. Chen, K. Sasaki, C. Ma, A. I. Frenkel, N. Marinkovic, J. T. Muckerman, Y. Zhu, R. R. Adzic, *Angew. Chem. Int. Ed.* **2012**, *51*, 6131–6135; *Angew. Chem.* **2012**, *124*, 6235–6239.

[64] Y. Abghoui, E. Skúlason, *J. Phys. Chem. C* **2017**, *121*, 24036–24045.

[65] Y. Zhang, B. Ouyang, J. Xu, G. Jia, S. Chen, R. S. Rawat, H. J. Fan, *Angew. Chem. Int. Ed.* **2016**, *55*, 8670–8674; *Angew. Chem.* **2016**, *128*, 8812–8816.

[66] Y. Zhu, G. Chen, X. Xu, G. Yang, M. Liu, Z. Shao, *ACS Catal.* **2017**, *7*, 3540–3547.

[67] R. Michalsky, Y.-J. Zhang, A. A. Peterson, *ACS Catal.* **2014**, *4*, 1274–1278.

[68] I. Matanovic, F. H. Garzon, *Phys. Chem. Chem. Phys.* **2018**, *20*, 14679–14687.

[69] Y. Liu, G. Yu, G. D. Li, Y. Sun, T. Asefa, W. Chen, X. Zou, *Angew. Chem. Int. Ed.* **2015**, *54*, 10752–10757; *Angew. Chem.* **2015**, *127*, 10902–10907.

[70] Z. W. Seh, K. D. Fredrickson, B. Anasori, J. Kibsgaard, A. L. Strickler, M. R. Lukatskaya, Y. Gogotsi, T. F. Jaramillo, A. Vojvodic, *ACS Energy Lett.* **2016**, *1*, 589–594.

[71] W. F. Chen, C. H. Wang, K. Sasaki, N. Marinkovic, W. Xu, J. T. Muckerman, Y. Zhu, R. R. Adzic, *Energy Environ. Sci.* **2013**, *6*, 943.

[72] R. Ma, Y. Zhou, Y. Chen, P. Li, Q. Liu, J. Wang, *Angew. Chem. Int. Ed.* **2015**, *54*, 14723–14727; *Angew. Chem.* **2015**, *127*, 14936–14940.

[73] J. Xiong, J. Li, J. Shi, X. Zhang, W. Cai, X. Lei, L. Feng, Z. Yang, L. Huang, H. Cheng, *ACS Energy Lett.* **2018**, *3*, 341–348.

[74] Y. Huang, J. Ge, J. Hu, J. Zhang, J. Hao, Y. Wei, *Adv. Energy Mater.* **2018**, *8*, 1701601.

[75] C. Tang, W. Wang, A. Sun, C. Qi, D. Zhang, Z. Wu, D. Wang, *ACS Catal.* **2015**, *5*, 6956–6963.

[76] L. Liao, S. Wang, J. Xiao, X. Bian, Y. Zhang, M. D. Scanlon, X. Hu, Y. Tang, B. Liu, H. H. Girault, *Energy Environ. Sci.* **2014**, *7*, 387–392.

[77] Y. T. Xu, X. Xiao, Z. M. Ye, S. Zhao, R. Shen, C. T. He, J. P. Zhang, Y. Li, X. M. Chen, *J. Am. Chem. Soc.* **2017**, *139*, 5285–5288.

[78] P. Xiao, X. Ge, H. Wang, Z. Liu, A. Fisher, X. Wang, *Adv. Funct. Mater.* **2015**, *25*, 1520–1526.

[79] M. M. Najafpour, G. Renger, M. Holynska, A. N. Moghaddam, E. M. Aro, R. Carpentier, H. Nishihara, J. J. Eaton-Rye, J. R. Shen, S. I. Allakhverdiev, *Chem. Rev.* **2016**, *116*, 2886–2936.

[80] M. Carmo, D. L. Fritz, J. Mergel, D. Stolten, *Int. J. Hydrogen Energy* **2013**, *38*, 4901–4934.

[81] D. M. F. Santos, C. A. C. Sequeira, J. L. Figueiredo, *Química Nova.* **2013**, *36*, 1176–1193.

[82] M. D. Merrill, R. C. Dougherty, *J. Phys. Chem. C* **2008**, *112*, 3655–3666.

[83] C. C. McCrory, S. Jung, I. M. Ferrer, S. M. Chatman, J. C. Peters, T. F. Jaramillo, *J. Am. Chem. Soc.* **2015**, *137*, 4347–4357.

[84] J. Staszak-Jirkovský, C. D. Malliakas, P. P. Lopes, N. Danilovic, S. S. Kota, K. C. Chang, B. Genorio, D. Strmcnik, V. R. Stamenkovic, M. G. Kanatzidis, N. M. Markovic, *Nat. Mater.* **2016**, *15*, 197–203.

[85] J. Zhang, T. Wang, P. Liu, Z. Q. Liao, S. H. Liu, X. D. Zhuang, M. W. Chen, E. Zschech, X. L. Feng, *Nat. Comm.* **2017**, *8*, 15437.

[86] E. A. Paoli, F. Masini, R. Frydendal, D. Deiana, C. Schlaup, M. Malizia, T. W. Hansen, S. Horch, I. E. L. Stephens, I. Chorkendorff, *Chem. Sci.* **2015**, *6*, 190–196.

[87] S. Chen, T. Takata, K. Domen, *Nat. Rev. Mater.* **2017**, *2*, 17050.

[88] G. Halpert, *J. Power Sources* **1984**, *12*, 177–192.

[89] D. A. Corrigan, *J. Electrochem. Soc.* **1987**, *134*, 377.

[90] M. Gong, Y. Li, H. Wang, Y. Liang, J. Z. Wu, J. Zhou, J. Wang, T. Regier, F. Wei, H. Dai, *J. Am. Chem. Soc.* **2013**, *135*, 8452–8455.

[91] M. W. Louie, A. T. Bell, *J. Am. Chem. Soc.* **2013**, *135*, 12329–12337.

[92] L. Trotochaud, J. K. Ranney, K. N. Williams, S. W. Boettcher, *J. Am. Chem. Soc.* **2012**, *134*, 17253–17261.

[93] L. Trotochaud, S. L. Young, J. K. Ranney, S. W. Boettcher, *J. Am. Chem. Soc.* **2014**, *136*, 6744–6753.

[94] T. N. Lambert, J. A. Vigil, S. E. White, D. J. Davis, S. J. Limmer, P. D. Burton, E. N. Coker, T. E. Beechem, M. T. Brumbach, *Chem. Commun.* **2015**, *51*, 9511–9514.

[95] J. Tian, N. Cheng, Q. Liu, X. Sun, Y. He, A. M. Asiri, *J. Mater. Chem. A* **2015**, *3*, 20056–20059.

[96] I. Roger, M. A. Shipman, M. D. Symes, *Nat. Chem. Rev.* **2017**, *1*, 0003.

[97] M. Pourbaix, *Atlas of Electrochemical Equilibria in Aqueous Solutions*, Pergamon, New York, **1966**.

[98] J. Y. Chen, J. T. Miller, J. B. Gerken, S. S. Stahl, *Energy Environ. Sci.* **2014**, *7*, 1382.

[99] J. Wang, W. Cui, Q. Liu, Z. Xing, A. M. Asiri, X. Sun, *Adv. Mater.* **2016**, *28*, 215–230.

[100] N. H. Chou, P. N. Ross, A. T. Bell, T. D. Tilley, *ChemSusChem.* **2011**, *4*, 1566–1569.

[101] X. Zou, A. Goswami, T. Asefa, *J. Am. Chem. Soc.* **2013**, *135*, 17242–17245.

[102] L. Han, S. Dong, E. Wang, *Adv. Mater.* **2016**, *28*, 9266–9291.

[103] P. C. K. Vesborg, T. F. Jaramillo, *RSC Adv.* **2012**, *2*, 7933.

[104] M. W. Kanan, Y. Surendranath, D. G. Nocera, *Chem. Soc. Rev.* **2009**, *38*, 109–114.

[105] Y. Surendranath, M. W. Kanan, D. G. Nocera, *J. Am. Chem. Soc.* **2010**, *132*, 16501–16509.

[106] A. J. Esswein, Y. Surendranath, S. Y. Reece, D. G. Nocera, *Energy Environ. Sci.* **2011**, *4*, 499–504.

[107] S. H. Hsu, J. Miao, L. Zhang, J. Gao, H. Wang, H. Tao, S. F. Hung, A. Vasileff, S. Z. Qiao, B. Liu, *Adv. Mater.* **2018**, *30*, 1707261.

[108] J. S. Mondschein, J. F. Callejas, C. G. Read, J. Y. Chen, C. F. Holder, C. K. Badding, R. E. Schaak, *Chem. Mater.* **2017**, *29*, 950–957.

[109] M. Blasco-Ahicart, J. Soriano-Lopez, J. J. Carbo, J. M. Poblet, J. R. Galan-Mascaros, *Nat. Chem.* **2017**, *10*, 24 – 30.
[110] J. E. Turner, *J. Electrochem. Soc.* **1984**, *131*, 1777.
[111] I. Cesar, A. Kay, J. A. Gonzalez Martinez, M. Gratzel, *J. Am. Chem. Soc.* **2006**, *128*, 4582 – 4583.
[112] M. S. Burke, S. Zou, L. J. Enman, J. E. Kellon, C. A. Gabor, E. Pledger, S. W. Boettcher, *J. Phys. Chem. Lett.* **2015**, *6*, 3737 – 3742.
[113] S. Zou, M. S. Burke, M. G. Kast, J. Fan, N. Danilovic, S. W. Boettcher, *Chem. Mater.* **2015**, *27*, 8011 – 8020.
[114] J. A. Seabold, K. S. Choi, *J. Am. Chem. Soc.* **2012**, *134*, 2186 – 2192.
[115] G. Liu, J. Shi, F. Zhang, Z. Chen, J. Han, C. Ding, S. Chen, Z. Wang, H. Han, C. Li, *Angew. Chem. Int. Ed.* **2014**, *53*, 7295 – 7299; *Angew. Chem.* **2014**, *126*, 7423 – 7427.
[116] G. Liu, S. Ye, P. Yan, F. Xiong, P. Fu, Z. Wang, Z. Chen, J. Shi, C. Li, *Energy Environ. Sci.* **2016**, *9*, 1327 – 1334.
[117] J. E. Post, *Proc. Natl. Acad. Sci. USA* **1999**, *96*, 3447 – 3454.
[118] G. Renger, *Biochim. Biophys. Acta Bioenerg.* **2012**, *1817*, 1164 – 1176.
[119] G. W. Brudvig, *Philos. Trans. R. Soc. London Ser. B* **2008**, *363*, 1211 – 128 discussion 1218 – 1219.
[120] J. J. Concepcion, M. K. Tsai, J. T. Muckerman, T. J. Meyer, *J. Am. Chem. Soc.* **2010**, *132*, 1545 – 1557.
[121] M. D. Symes, Y. Surendranath, D. A. Lutterman, D. G. Nocera, *J. Am. Chem. Soc.* **2011**, *133*, 5174 – 5177.
[122] Y. Meng, W. Song, H. Huang, Z. Ren, S. Y. Chen, S. L. Suib, *J. Am. Chem. Soc.* **2014**, *136*, 11452 – 11464.
[123] T. Takashima, K. Hashimoto, R. Nakamura, *J. Am. Chem. Soc.* **2012**, *134*, 1519 – 1527.
[124] T. Takashima, K. Hashimoto, R. Nakamura, *J. Am. Chem. Soc.* **2012**, *134*, 18153 – 18156.
[125] M. Huynh, D. K. Bediako, D. G. Nocera, *J. Am. Chem. Soc.* **2014**, *136*, 6002 – 6010.
[126] R. Frydendal, E. A. Paoli, I. Chorkendorff, J. Rossmeisl, I. E. L. Stephens, *Adv. Energy Mater.* **2015**, *5*, 1500991.
[127] J. Hwang, R. R. Rao, L. Giordano, Y. Katayama, Y. Yu, Y. Shao-Horn, *Science* **2017**, *358*, 751 – 756.
[128] Y. Matsumoto, J. Kurimoto, E. Sato, *J. Electron. Chem. Interfacial Electrochem.* **1979**, *102*, 77 – 83.
[129] Y. Matsumoto, *J. Electrochem. Soc.* **1980**, *127*, 2360.
[130] J. Suntivich, K. J. May, H. A. Gasteiger, J. B. Goodenough, Y. Shao-Horn, *Science* **2011**, *334*, 1383 – 1385.
[131] W. T. Hong, R. E. Welsch, Y. Shao-Horn, *J. Phys. Chem. C* **2016**, *120*, 78 – 86.
[132] S. Royer, D. Duprez, F. Can, X. Courtois, C. Batiot-Dupeyrat, S. Laassiri, H. Alamdari, *Chem. Rev.* **2014**, *114*, 10292 – 10368.
[133] A. Heel, P. Holtappels, P. Hug, T. Graule, *Fuel Cells* **2010**, *10*, 419 – 432.
[134] E. Fabbri, M. Nachtegaal, T. Binninger, X. Cheng, B. J. Kim, J. Durst, F. Bozza, T. Graule, R. Schaublin, L. Wiles, M. Pertoso, N. Danilovic, K. E. Ayers, T. J. Schmidt, *Nat. Mater.* **2017**, *16*, 925 – 931.
[135] T. Binninger, R. Mohamed, K. Waltar, E. Fabbri, P. Levecque, R. Kotz, T. J. Schmidt, *Sci. Rep.* **2015**, *5*, 12167.
[136] B. A. Pinaud, J. D. Benck, L. C. Seitz, A. J. Forman, Z. Chen, T. G. Deutsch, B. D. James, K. N. Baum, G. N. Baum, S. Ardo, H. Wang, E. Miller, T. F. Jaramillo, *Energy Environ. Sci.* **2013**, *6*, 1983.
[137] A. Heller, *Pure Appl. Chem.* **1986**, *58*, 1189 – 1192.
[138] S. Hu, M. R. Shaner, J. A. Beardslee, M. Lichterman, B. S. Brunschwig, N. S. Lewis, *Science* **2014**, *344*, 1005 – 1009.
[139] J. J. Pijpers, M. T. Winkler, Y. Surendranath, T. Buonassisi, D. G. Nocera, *Proc. Natl. Acad. Sci. USA* **2011**, *108*, 10056 – 10061.
[140] T. Yao, R. Chen, J. Li, J. Han, W. Qin, H. Wang, J. Shi, F. Fan, C. Li, *J. Am. Chem. Soc.* **2016**, *138*, 13664 – 13672.
[141] J. R. McKone, N. S. Lewis, H. B. Gray, *Chem. Mater.* **2014**, *26*, 407 – 414.
[142] J. D. Benck, B. A. Pinaud, Y. Gorlin, T. F. Jaramillo, *PLoS One* **2014**, *9*, e107942.
[143] K. Zeng, D. Zhang, *Prog. Energy Combust. Sci.* **2010**, *36*, 307 – 326.
[144] D. Deng, K. S. Novoselov, Q. Fu, N. Zheng, Z. Tian, X. Bao, *Nat. Nanotechnol.* **2016**, *11*, 218 – 230.
[145] J. Deng, P. Ren, D. Deng, L. Yu, F. Yang, X. Bao, *Energy Environ. Sci.* **2014**, *7*, 1919 – 1923.
[146] X. Zou, X. Huang, A. Goswami, R. Silva, B. R. Sathe, E. Mikmekova, T. Asefa, *Angew. Chem. Int. Ed.* **2014**, *53*, 4372 – 4376; *Angew. Chem.* **2014**, *126*, 4461 – 4465.
[147] J. Zhang, P. Liu, G. Wang, P. P. Zhang, X. D. Zhuang, M. W. Chen, I. M. Weidinger, X. L. Feng, *J. Mater. Chem. A* **2017**, *5*, 25314 – 25318.
[148] S. Han, Y. Feng, F. Zhang, C. Yang, Z. Yao, W. Zhao, F. Qiu, L. Yang, Y. Yao, X. Zhuang, X. Feng, *Adv. Funct. Mater.* **2015**, *25*, 3899 – 3906.
[149] Z. Yao, Y. Su, C. Lu, C. Yang, Z. Xu, J. Zhu, X. Zhuang, F. Zhang, *New J. Chem.* **2016**, *40*, 6015 – 6021.
[150] C. Lu, D. Tranca, J. Zhang, F. N. Rodriguez Hernandez, Y. Su, X. Zhuang, F. Zhang, G. Seifert, X. Feng, *ACS Nano* **2017**, *11*, 3933 – 3942.
[151] M. Cai, F. Zhang, C. Zhang, C. Lu, Y. He, Y. Qu, H. Tian, X. Feng, X. Zhuang, *J. Mater. Chem. A* **2018**, *6*, 138 – 144.
[152] C. Spöri, J. T. H. Kwan, A. Bonakdarpour, D. P. Wilkinson, P. Strasser, *Angew. Chem. Int. Ed.* **2017**, *56*, 5994 – 6021; *Angew. Chem.* **2017**, *129*, 6088 – 6117.

Manuscript received: July 22, 2018
Revised manuscript received: August 29, 2018
Accepted manuscript online: September 9, 2018
Version of record online: November 21, 2018